# Development of a compact focus variation microscopy sensor for on-machine surface topography measurement

**Teguh Santoso[1*], Wahyudin P. Syam[1§], Subbareddy Darukumalli[1], Richard Leach[1]**
[1]Manufacturing Metrology Team, Faculty of Engineering, University of Nottingham, UK

Corresponding authors:
*Teguh.Santoso@nottingham.ac.uk
§Wahyudin.Syam@nottingham.ac.uk

**Abstract.** On-machine areal surface topography measuring instruments are required for fast and accurate measurement of parts inside production machines without reducing production rates. This paper presents the design and development of a compact focus variation microscopy sensor that can be integrated into various types of machine tools. The paper focuses on the development of the linear stage of the sensor, which was the major engineering challenge. The overall developed sensor has dimensions of 78 mm diameter and 200 mm length, with a 20 mm travel range. Simulations of tolerance stack-ups for the sensor assembly were performed before the manufacturing of the sensor's linear motion components to assure they can be appropriately assembled. The linear motion accuracy of the sensor is 2 μm, calibrated using laser interferometry. From measurement in a controlled laboratory, the measurement noise of the sensor is 0.4 μm. Finally, demonstrations of calibrated artefact measurements with the sensor are presented. A single image field measurement with the sensor requires less than 20 s.

**Keywords:** On-machine sensor, Focus variation, Surface texture, Precision engineering, Motion stage

## 1. Introduction

On-machine measurements are required for fast and accurate defect inspection in manufacturing systems without reducing production rates [1-4]. On-machine measurement is a form of measurement that is performed inside a production machine. Meanwhile, Off-line measurement is any measurement that is not synchronised with a manufacturing line, it is conducted outside the manufacturing environment, such as in an environmentally well-controlled laboratory. With on-machine measurement, measurement data can be used as part of closed-loop feedback for both process control and optimisation at each stage (pre-process, in-process or post-process) of the production chain [5]. There have recently been several developments of on-machine optical measuring instruments, for example, see references [6-10]. On-machine optical measuring instruments can be classified based on their data acquisition methods, which are single point [7,9,10] and full-field [8]. In a single point method, a single point displacement probe is moved by an actuator which is commonly the moving stage of the machine tool or by an additional precision linear stage [7,9,10]. The single point displacement probe scans a surface continuously acquiring 3D points then reconstructs the surface topography by applying a surface reconstruction algorithm. For the full-field method, the instrument can capture a surface area within its field of view then reconstructs the surface topography. This full-field method is faster than the single point method. Many applications of on-machine optical measuring instruments are designed for a specific machine tool and cannot be integrated for other types of machine tool. For example, Graves et al. [6] discussed several optical measurement methods integrated at fabrication sites that produce large

area high precision freeform surface optics used for telescopes. The use of four displacement measurement probes that are employed into a large-scale drum-roll lathe machine has been proposed [7]. Many developments of optical instrument for on-machine measurements are still at the prototype stage and are not ready for full integration into machine tools due to, for example, the requirement for additional setups and modules to conform with the machine tool environments [7-10].

The effects of vibration and temperature variation are significant in on-machine measurements and can reduce the accuracy of measurement results. Strategies to reduce vibration noise are to minimise vibration sources, isolate the vibration sources and/or isolate the instrument. Vibration isolation can be realised by optimising the mechanical structure of the instrument, such as employing lattice-structures produced by additive manufacturing (AM) [11,12]. Another strategy is to compensate the vibrational effect, for example, a piezo-electric transducer has been used for an on-machine wavelength scanning interferometer to compensate the fluctuations in the optical path length caused by vibration from the surrounding environment [13]. For temperature variation, applying a controlled climate chamber has been proposed so that a desired thermal static condition can be acquired during on-machine measurements [14,15]. In addition, to ensure the traceability of on-machine measurement instruments, calibration procedures need to quantify the uncertainty contributions due to these environmental noise sources [9,16,17].

Off-line focus variation microscopy (FVM) has become one of common optical instruments for measuring surface topography [18,19]. There are several publications that use FVM for characterisation of the surface quality of parts produced by additive manufacturing (AM) process [20-25], characterisation of the wear at the leading edge of a compressor blade [26] and characterisation of tool wear in machining [27]. Another report shows the integration of a commercial FVM sensor into a laser processing machine to measure the diameter of high aspect ratio micro-holes produced by a two-sided laser processing method [28]. Additionally, the integration of a commercial FVM sensor mounted on a collaborative robot has been reported [29]. This integration enables the measurement of features with micro-geometries on a large high precision part. FVM is relatively robust to low frequency vibration such as ground vibration. This robustness makes FVM as potential solution for on-machine measurement for defect inspection and quality control of micro-scale parts [4,30].

FVM requires an accurate motion stage to perform high-accuracy measurements. Many technologies for positioning systems are found in ultra-precision machine tools and coordinate measuring machines (CMMs) [31-34]. There are two factors that significantly influence the positioning accuracy of motion stages: errors due to geometrical and thermo-mechanical variations [34,35]. Geometrical errors are caused by the imperfect shape and load-induced deformation of components that constitute the structure and sliding mechanism of the motion stage. These geometric errors can be minimised by, for example, minimising Abbe offsets [36,37], separating the force and metrology loops of the stage [38,39], implementing motion error compensation [40] and using ultra-low friction air-bearings or hydrostatic bearings for sliding mechanisms [31]. Thermo-mechanical errors are due to temperature changes that cause the structures or parts constituting the motion stage to change dimension. Reducing thermo-mechanical errors can be carried out by using materials of low coefficient of thermal expansion for the critical structures, applying thermally-induced motion error compensation and placing the machine or instrument in a temperature-controlled environment [14,41].

Most on-machine measuring instruments are designed for specific machine and are not flexible. Also, very often, those instruments are made for either geometrical or surface texture measurements. Currently, there is a need for general-purpose on-machine measuring instruments that can measure both micro-scale geometry and surface texture and be integrated into various production machines.

The aim of the research reported here is to design and develop a novel compact FVM sensor for on-machine measurement and can be integrated into various machine tools. The definition of the term "on-machine" follows that developed as part of a recent UK roadmap [42], i.e. measurement performed inside a production machine or manufacturing line. To construct the sensor, a new high-accuracy, small and compact linear motion stage has been developed. The design of the compact linear motion stage

follows Abbe compliant principles, has predetermined target accuracy and motion range requirements, can be mounted in various sizes of machine tool chambers and tool holders in harsh environmental conditions, and is relatively cost efficient.

This paper is structured as follows. Section 2 describes the detailed requirements of the compact FVM sensor. Section 3 presents the conceptual design, system diagram, detailed design model including the finite element analysis and assembly of the sensor. Section 4 presents the tolerance stack-up modelling to analyse the geometrical variation of the sensor assembly as well as the geometrical verification using a CMM. Motion accuracy verification using a laser interferometer is presented in section 5. Section 6 demonstrates the compact FVM sensor's capability to measure a reference artefact and compares the results with an off-line FVM instrument. Section 7 concludes the paper and discusses future work.

## 2. Requirements on the compact FVM sensor

FVM is an optical surface topography measurement method where the sharpness of a surface image at optimal focus positions in axial direction is used to determine the surface height. Figure 1 shows the maximum sharpness (focus value) that indicates the height of a reconstructed surface at lateral position $(x,y)$ of a surface image within the field of view (FOV) of the measured surface. A stack of surface images is captured by an image sensor within an optical microscope during axial scanning. The maximum focus value at each lateral position is determined by comparing it with its neighbours. After detecting the maximum focus value for all lateral positions in each stack of surface images, a depth map can be constructed. Different lateral resolutions and FOVs can be acquired through different objectives. More detailes about the calculation of a focus value are given elsewhere [19,43].
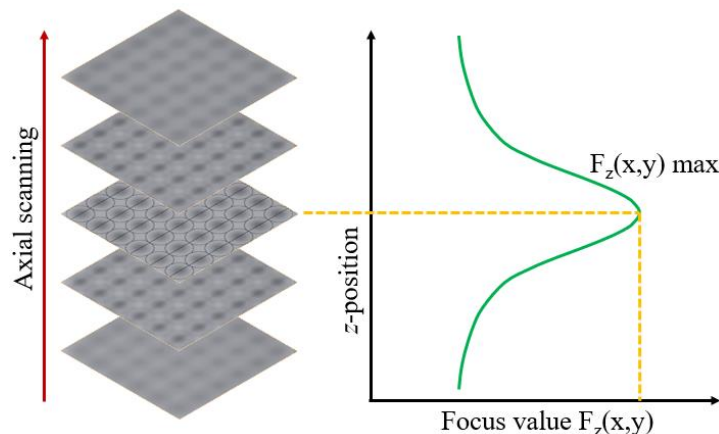


**Figure 1.** The FVM method [43].

The ability of the FVM sensor to measure micro-scale features accurately is determined by the performance of the linear stage. The optical tube of the sensor is mounted on the linear stage, allowing accurate and precise axial scanning along the optical axis. For this development, the requirements for the overall sensor and the linear stage have been defined based on the consideration of the desired measurement accuracy, the typical dimensions of features to be measured, the combination of the tool holder and the cutting tool allowed in tool changer system and volume of the machining chamber for various micro-scale milling machines, thus:

- Maximum travel is 20 mm.
- Encoder resolution is less than 25 nm.
- Positioning accuracy is less than 1 μm.
- Positioning repeatability is less than 250 nm.
- Maximum overall cylindrical dimensions are 80 mm diameter and 250 mm length.

The overall maximum dimensions of the FVM sensor are mainly determined to fit into various machine tool chambers. The dimensions of designed and off-the-shelf components are configured so that they fit within the maximum specified overall dimensions. The components are machined parts for the structure, ball-screw, linear bearing, ball-bearing, motor, linear encoder, objective lens, tube lens and electronics for the control system. The use of off-the-shelf components reduces the total manufacturing cost of the sensor.

## 3. Compact FVM sensor

### 3.1 Conceptual design

The design of the compact sensor complies with the Abbe principle, in that it minimises the Abbe offset [34,38]. The Abbe principle requires the line of the effective point (EP) of the displacement measurement system of the sensor to be collinear with the line of the functional point (FP) whose displacement is to be measured [34,38]. This requirement implies that the displacement between the two axis vectors should be zero or as small as possible. Therefore, errors associated with the angular deviation between the axes of the EP and FP should be minimised. The FP of the compact FVM sensor is designed such that it is co-axial with the axis of the optical system. The displacement measurement system (linear encoder) of the sensor is configured such that its axis coincides with the axis of the optical system. The EP of the linear encoder is the readout position on the measuring scale. The design configuration of the sensor is illustrated in figure 2.
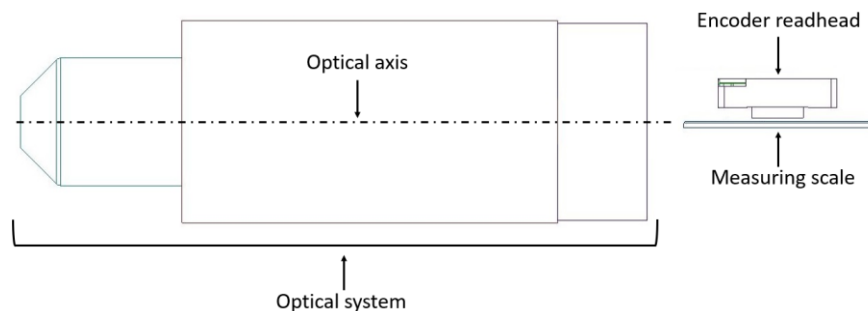


**Figure 2.** The configuration of the optical system and the linear encoder such that the axis of the FP and the EP are co-axial.

To minimise the overall manufacturing cost of the sensor's structure, we consider the selection of materials, the design of the structure's geometries and the allocated tolerance values so that the parts can be machined efficiently while facilitating the assembly of the sensor. The main assembly characteristics are to minimise the offset and misalignment between the measuring scale axis and optical axis of the sensor. An optimal tolerance allocation for the machined parts can be achieved by performing a tolerance variation chain analysis [44] (see section 3.5 for the detailed tolerance analysis of the sensor components and assembly).

### 3.2 System schema

Figure 3 shows a conceptual schema of the FVM sensor. The optical and drivetrain components are connected to a computer and electronic system. The optical system setup is composed of a complementary metal-oxide-semiconductor (CMOS) sensor equipped with universal serial bus (USB) 3.0, the configuration of a tube lens and a $10\times$ objective lens with specific focal length resulting a FOV of $(1.7 \times 1.7)$ mm and an off-axis ring light positioned alongside the objective lens. To achieve a compact design of the sensor, coaxial illumination is not applied (a larger number of lens components would be required for coaxial illumination). An industrial general motion controller controls the motor based on the feedback signal from the linear encoder with a resolution of 20 nm. The motor torque output is converted to a linear response to move the carriage. During the scanning along the axis of the optical

system, the CMOS sensor and the motion controller that are connected to the mini-computer captures image data and axial position respectively. Then image data and axial position are ready for a pre-processing phase. This phase is the first step in reconstructing the areal surface topography, and is typically used to remove noise on the raw data. Then the pre-processed data are sent to a workstation for further surface reconstruction and characterisation.
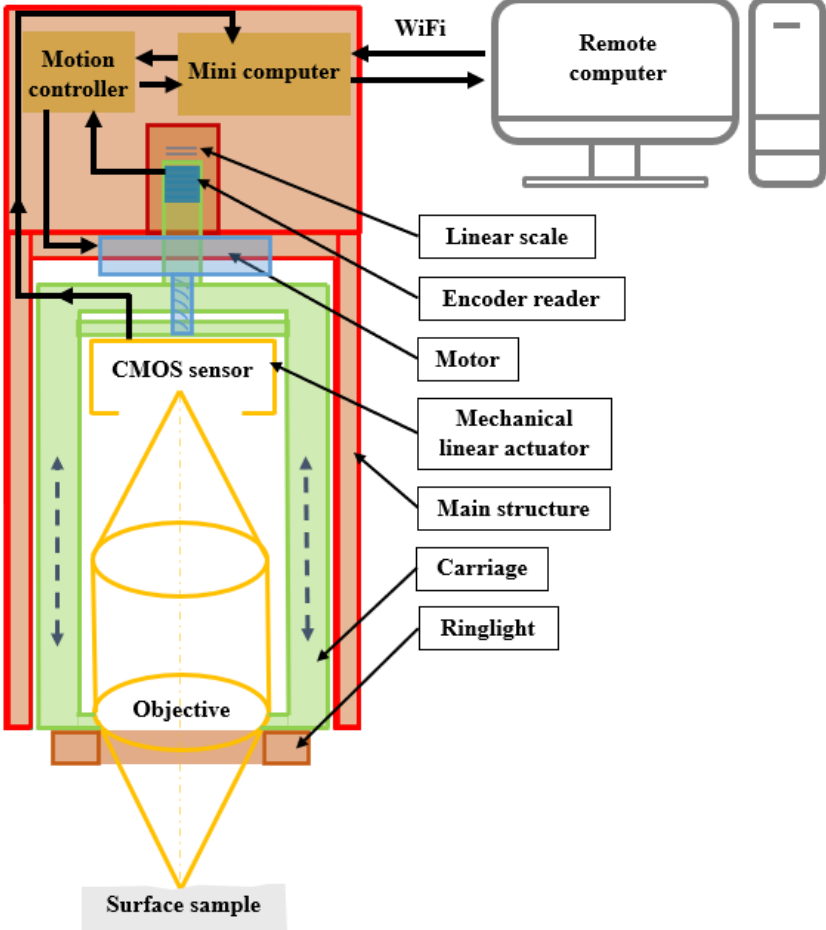


**Figure 3.** System schema of the compact FVM sensor.

*3.3 Design of the compact FVM sensor*

The 3D model of the sensor assembly (mechanical system and optical components) is shown in figure 4. The sensor is designed to have a 20 mm travel range and a mounting thread that fits to common machine tool holders. The placement of the linear encoder is configured such that the optical axis and the linear scale axis are coincident to minimise Abbe error. The Abbe error originates from the Abbe offset, in this case, caused by the assembly of imperfectly manufactured components that constitute the structure and mounting of the optical system, the motion system and the linear scale. The larger the axis offset between the measuring scale (EP) and the optical axis (FP), the larger the Abbe offset, and the larger the resulting error.
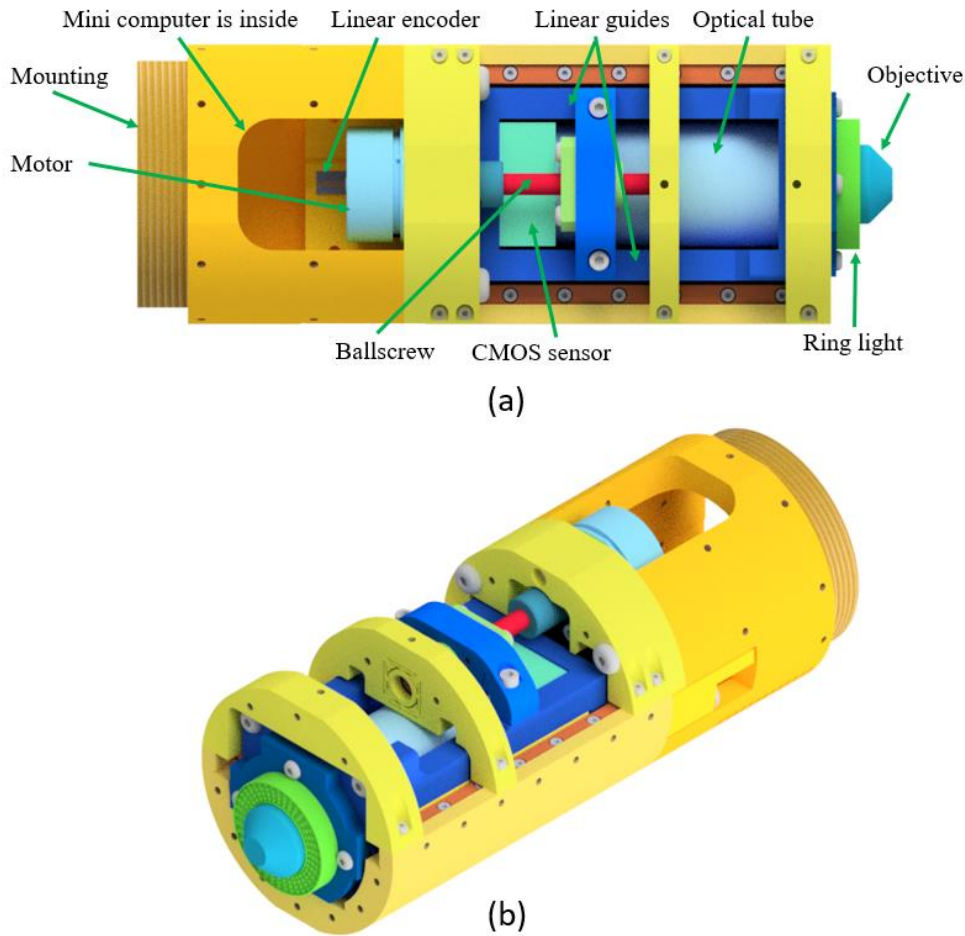
**Figure 4.** (a). Top view of 3D model of the compact FVM sensor. (b). Isometric view of 3D model of the compact FVM sensor.

The design of the compact FVM sensor separates the force and metrological loops to prevent distortion of the components in the force loop due to, for example, loads due to gravitation, thermal expansion and the mass of the optical setup [34,38,39]. This distortion affects the components in the metrology loops. The separation of the two loops is achieved by separating the mounting of the optics holder and carriage and, the mounting of the measuring scale and the reading head of the linear encoder. The force loop and the metrology loop of the developed sensor are shown in figure 5. From figure 5(a), the force loop goes through the ballscrew, support frame of the carriage, linear guides, the base frame and back to the motor frame. And from figure 5(b), the metrology loop goes through the gap between the reading head interface and the measuring scale placed on the metrology frame, the reading head frame, support frame of the carriage, linear guides, the base frame and back to the linear encoder frame. However, there is a small area in which both force and metrology loops pass together on the linear guides and the base frame, then split into different structures, as shown in figure 5(c). The effect of the force loop, in the form of vibration, to the small area is considered relatively small, due to the use of a brushless direct current (DC) motor and very slow scanning speeds during measurement (below 250 µm/s).

The design of the sensor is symmetrical to provide several benefits [34,38,39], such as proportional distribution of the force and metrology loops (see the half section of the 3D assembly model in figure 5). With this symmetrical design, the variation of temperature, vibration and force generated

by the system will be evenly distributed. In addition, the system will remain stable under proportionally distributed mechanical deformation.
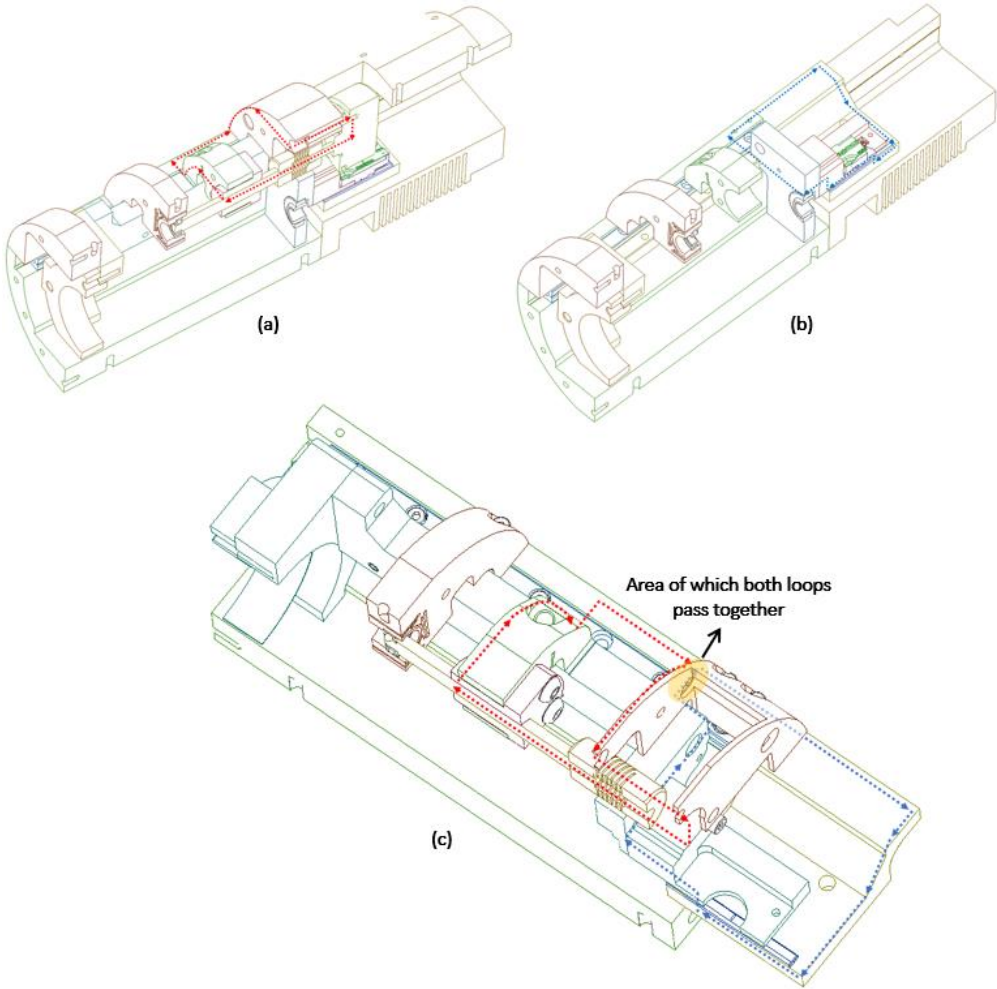


**Figure 5.** (a). Force loop, (b) metrology loop and (c) both loops of the developed sensor.

During the design iterations of the sensor, finite element analysis (FEA) was utilised to evaluate the mechanical structural behaviour of the system designs, such as deformation under load, the structure's rigidity and thermal deformation, and to optimise the designs. The main mechanical structures of the sensor are divided into the carriage structure and the frame structure. The design of the mechanical structure considers the manufacturability and the assembly the system. The structure's material is grade 416 stainless steel that has a coefficient of thermal expansion of $9.9 \times 10^{-6}$ K$^{-1}$ and thermal conductivity of 24.9 Wm$^{-1}$K$^{-1}$, therefore, offering relatively low thermal expansion for the sensor's structure. Moreover, due to its other properties, the natural frequency for the sensor is higher than the environmental vibration frequency while performing on-machine measurements [11,45]. FEA analyses were conducted using the commercial software ABAQUS, to estimate the mechanical structural behaviour under cases representing several measurement conditions of the sensor.

The mesh for the FEA model of the structure is shown in figure 6. The FEA model is meshed with linear hexahedral shaped elements and the assigned material is stainless steel AISI type 416. Convergence tests were performed for each simulation case to determine the appropriate numbers of elements that result in converged simulation results. In figure 6, a fixed point of the frame structure in the FEA model is shown and set to be attached to a tool holder.
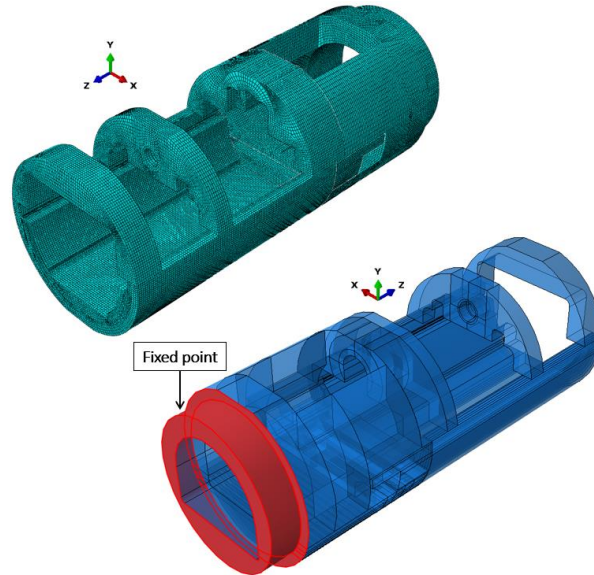


**Figure 6.** Frame structure model and its meshed model for the FEA vibration and heat transfer simulations.

Based on the geometrical shape of the frame structure and the associated materials, a modal analysis was performed to evaluate the natural frequencies (eigen frequencies) of the structure of the sensor. Different shapes and materials of the structure will significantly affect its natural frequency [11,45]. The goal of this simulation was to compare the natural frequency of the structure of the sensor with possible frequencies of vibration from the environment where the sensor will be used. The structure of the sensor is designed and optimised such that the peaks of its natural frequency in different modes are sufficiently far from the expected peaks of vibration from the environment [45]. The modal analysis simulation result of the structure is presented in figure 7, it can be seen that the first, second and third mode shapes, representing vibration in vertical, horizontal and rotational degrees of freedom respectively, occur at the extruded U-shape frame or part A. The lowest natural frequency at the first mode shape vibration is 874.6 Hz. The fourth mode shape occurs in part B and C (see figure 7) with a natural frequency of 2063.4 Hz.
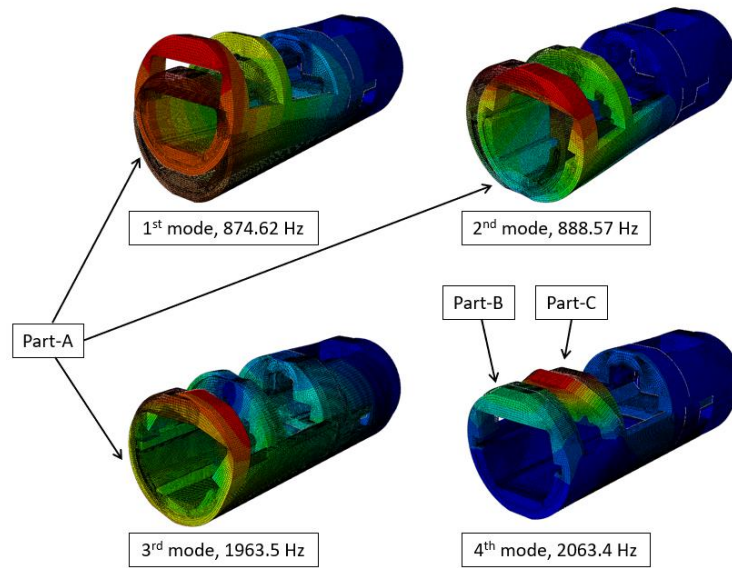
**Figure 7.** Mode shapes of the frame structure.

The structure of the compact FVM sensor will deform due to the heat transferred from the internal components of the sensor, such as the motor, mini-computer and camera, and from external sources, such as the heat generated from machine tool components. The heat is transferred mostly by conduction and convection. The deformation is caused by thermal stresses due to the distributed heat across the frame structure. This will potentially deform the metrology structure, where elements of the measurement system are mounted, such as the linear scale and its reading head, causing geometrical errors and degrading the positioning accuracy. Hence, evaluation of the temperature distribution and the generated thermal stresses across the frame structure is required to understand the deformation on the structure. FEA heat transfer simulations were performed, there are three heat transfer phenomena that were simulated representing the on-machine measurement conditions. Each phenomenon is simulated individually based on a specific circumstance. And we assume the measurement duration is 60 s, applied for phenomena two and three. These phenomena are described as follows:

1. Convection heat transfer occurs when the compact FVM sensor is placed inside the tool magazine of a machine tool. The temperature of the entire structure of the sensor equilibrates to the environmental temperature inside the tool magazine. A steady-state simulation was performed to calculate the deformation distribution of the frame structure. We assumed the environmental temperature and the natural convection coefficient inside the tool magazine are 23 °C and 4 Wm$^{-2}$K$^{-1}$, and the initial temperature of the frame structure is 20 °C. In this case, the steady-state condition of the frame structure will reach an equilibrium condition at 23 °C. With an increase of 3 °C of temperature of the frame structure, the simulated maximum deformation of the structure is 5.78 μm. This deformation distribution is shown in figure 8.

2. Convection heat transfer also occurs when the stored sensor inside the tool magazine is picked up and taken into the machining chamber to perform a measurement. The ambient temperature inside the machining chamber is higher than the ambient temperature inside the tool magazine. This temperature difference inevitably generates thermal stress on the frame structure. A transient simulation was performed to calculate the deformation distribution of the frame structure during the measurement. We assume the initial temperature of 23 °C is uniform throughout the entire frame structure, and the natural convection coefficient and the ambient temperature inside the machining chamber are 4 Wm$^{-2}$K$^{-1}$ and 25 °C respectively [46]. The simulation results show the maximum deformation is 0.11 μm and its deformation distribution is shown in figure 8.

3. Conduction heat transfer occurs from the heat generated from the motor and mini-computer. Based on the proposed 3D assembly model, there are two thermal sources generated from components

mounted on the frame structure. These components are the CMOS camera, motor and mini-computer that are active during measurement. The generated heat from the two thermal sources spreads throughout the frame structure by means of conductive heat transfer. The locations of the two thermal sources are shown in figure 9. A transient simulation was performed to calculate the deformation distribution of the frame structure due to the conductive heat transfer during a measurement. We assume the initial temperature of 23 °C is uniform throughout the entire frame structure and the temperature of the thermal sources increases with time (the temperature profile is shown in figure 9). The temperature profile is calculated based on the consideration that the motor and mini-computer are under a maximum workload. The simulation result shows that the maximum deformation is 11.45 μm and this is shown in figure 8.

Since one end of the frame structure is free, this section is the area where the maximum deformation is obtained from the FEA simulation for the three heat transfer scenarios (see figure 8). The convection and conduction heat transfer phenomena inside the machining chamber occur at the same time. From the simulation, the results show that the component deformations due to thermal stress resulting from convection heat transfer is much smaller than from the conduction. The maximum deformation due to convection is approximately only 1% of the deformation due to the conduction. The results suggest that there is a relatively low rate of heat transfer on the frame structure caused by the convection, which also lead to a relatively low rate of deformation. The maximum deformation of 5.78 μm due to convection occurs inside the tool magazine as a result of the steady-state simulation, which in reality, will take many hours to reach a uniform distribution temperature with respect to the environmental temperature. Contrary, the conductive heat transfer phenomenon shows a relatively high rate of deformation that occurs within less than fifteen minutes.
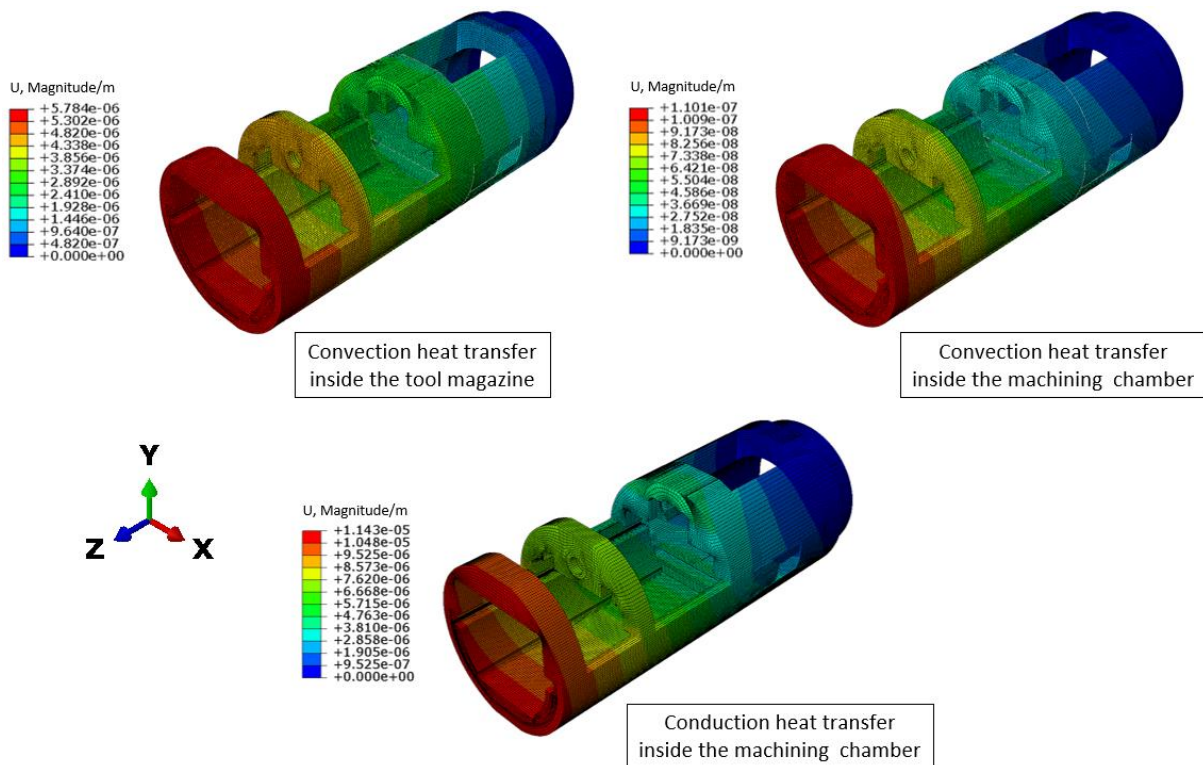


**Figure 8.** The frame structure deformation distribution affected by convection and conduction heat transfers.
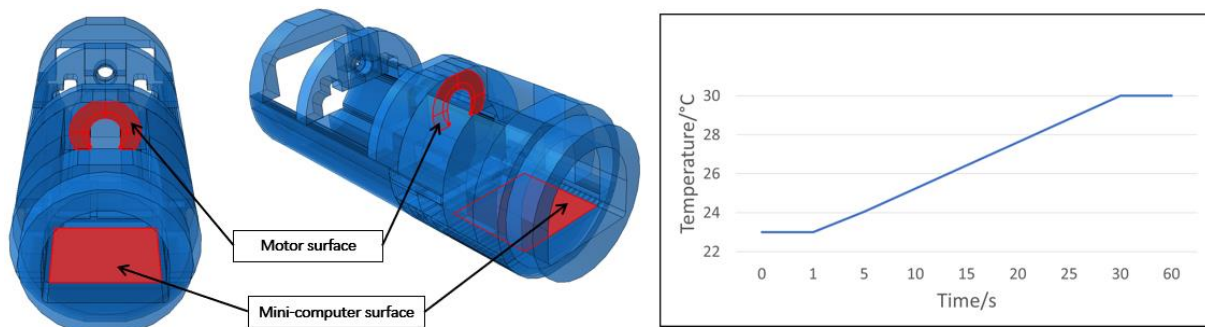
**Figure 9.** Thermal load locations and its temperature profile during the transient simulation.

*3.4 Assembly of the sensor prototype*

Normally, for precision assembly, the use of pin and hole features to guide the mating assembly of the structure's parts are used [44], and to machine such features are complex and require sufficient tight tolerances and therefore, this requires substantial machining cost. Hence, in our design, we defined datum features in such a way that the mating assembly of the structure's parts can be precisely positioned by exploiting the inherent surface on each part as the datum. All datums are defined based on the tolerance stack-up analysis performed in section 4. With these datum features, precision assembly can be achieved by utilising simple dial-gauges and gauge blocks. Figure 10 shows the full assembly of the carriage and frame structure with the drivetrain and optical systems.
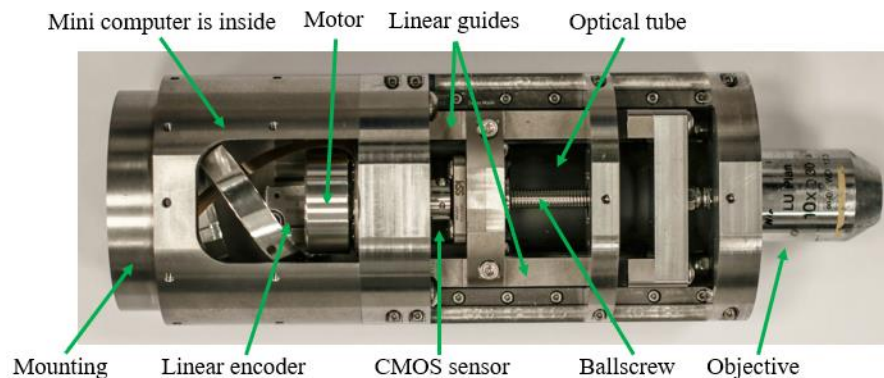


**Figure 10.** The full assembly of the sensor prototype.

## 4. Tolerance stack-up analysis of the compact FVM sensor

To understand the variation of key characteristics (KCs) of the compact FVM sensor assembly, a tolerance stack-up analysis was performed [44]. A KC is a defined function for an assembly so that the sensor's motion stage can operate as specified [44]. With this analysis, the geometrical variation of the final assembly of the sensor can be estimated before manufacturing the parts. In addition, the analysis can predict whether the variation is within the tolerance for the motion stage assembly to be functional. For example, the distance variation between the encoder reading head and linear scale of the sensor assembly should be within the range given by the manufacturer. The tolerance stack-up analysis was performed by calculating the propagation of the geometrical variation of parts involved in the KC chain. The geometrical variation was obtained from the defined geometrical and dimensional tolerances

allocated for each part on their engineering drawings. Due to commercial confidentiality, all tolerance values allocated for the parts used in tolerance stack-up analysis cannot be disclosed.

For the tolerance stack-up analysis, the propagation of variation from the components constructing the KCs is represented as a chain of reference frames moving from a feature on a part to another feature on the same or a different part. The chain is mathematically represented as multiplication of homogenous transformation matrices [47]. The transformation matrix $\mathbf{T_j^i}$ of the reference frame of a feature $i$ on a part to a feature $j$ on the same or a different part is formulated as:

$$\mathbf{T_j^i} = \begin{bmatrix} r_{11} & r_{12} & r_{13} & P_1 \\ r_{21} & r_{22} & r_{23} & P_2 \\ r_{31} & r_{32} & r_{33} & P_3 \\ 0 & 0 & 0 & 1 \end{bmatrix} \tag{1}$$

where $P$ is a translation feature and $r$ is a rotation feature. $\mathbf{T_j^i}$ represents the nominal reference frame transformation from feature $i$ to feature $j$. The transformation matrix $\mathbf{DT_i}$ of a reference frame of an imperfect (varying) feature $i$ on a part is formulated as:

$$\mathbf{DT_i} = \begin{bmatrix} 1 & -\delta\theta_z & \delta\theta_y & dx \\ \delta\theta_z & 1 & -\delta\theta_x & dy \\ -\delta\theta_y & \delta\theta_x & 1 & dz \\ 0 & 0 & 0 & 1 \end{bmatrix} \tag{2}$$

where $\delta\theta_x$ is the rotation feature along $x$-axis, $\delta\theta_y$ is the rotation feature along $y$-axis, $\delta\theta_z$ is the rotation feature along $z$-axis, $dx$ is the translation feature along $x$-axis, $dy$ is the translation feature along $y$-axis and $dz$ is the translation feature along $z$-axis. $\mathbf{DT_i}$ represents the variation of the reference frame transformation on feature $i$ due to part geometric errors allowed by the allocated tolerances.

*4.1 Key characteristics of the 3D assembly model and the tolerance chain*

There are two KCs, considered as the most critical attributes of the sensor assembly, that are analysed. The first KC is the plane angle deviation and distance between the reading head and the linear scale of the encoder (see figure 11), and the second KC is the offset and axis deviation between the optical axis system and measuring axis (see figure 12). The specified tolerances for all parts of the proposed 3D assembly model are based on key factors, such as the strategy of employed manufacturing techniques and the amount of allowed variation in the KCs. Due to the symmetrical design, the tolerance chains can be propagated through the left or the right side of the sensor structure. In this case, both the tolerance chains of the KCs are assumed propagating along the left side of the linear bearings of the sensor as illustrated in figure 13.
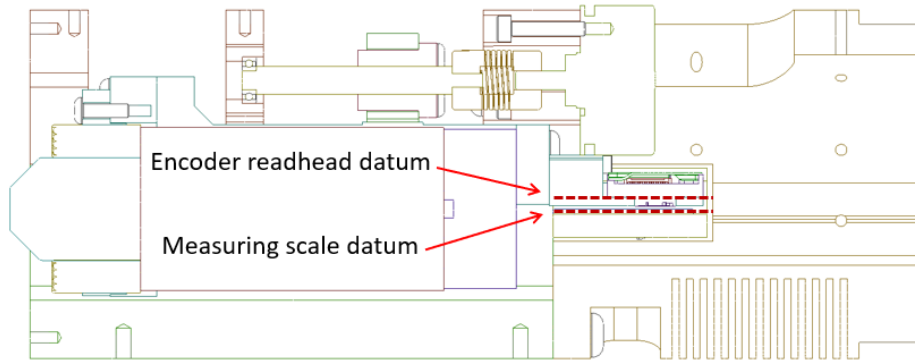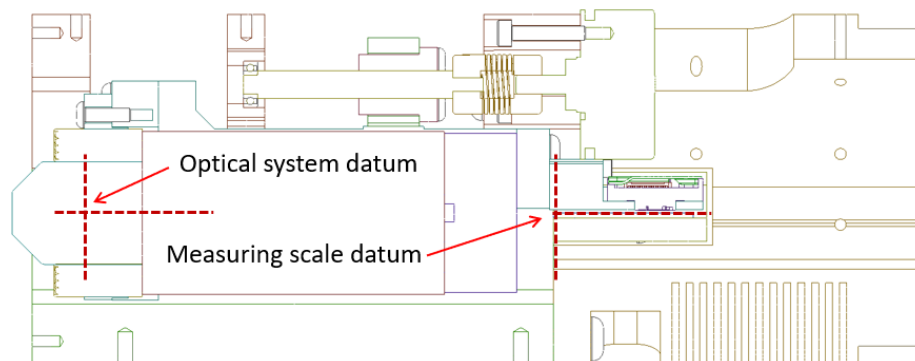
**Figure 11.** Illustration of the first KC.



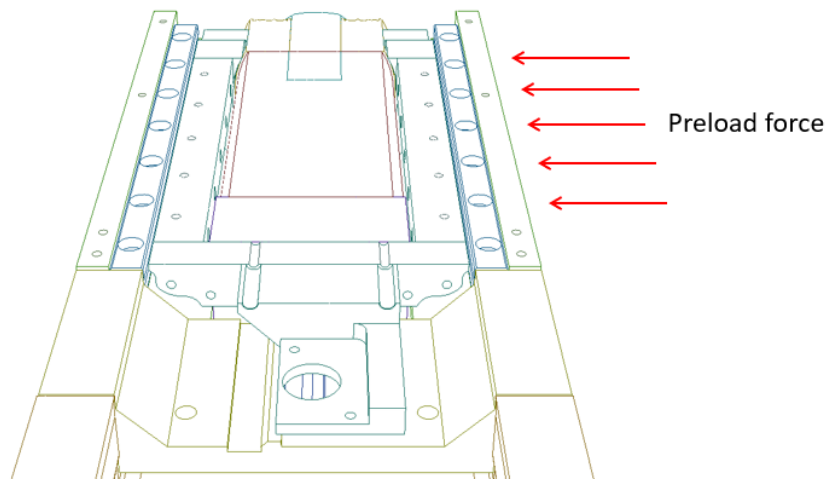**Figure 12.** Illustration of the second KC.



**Figure 13.** Illustration of the assumed preload direction for the linear bearings.
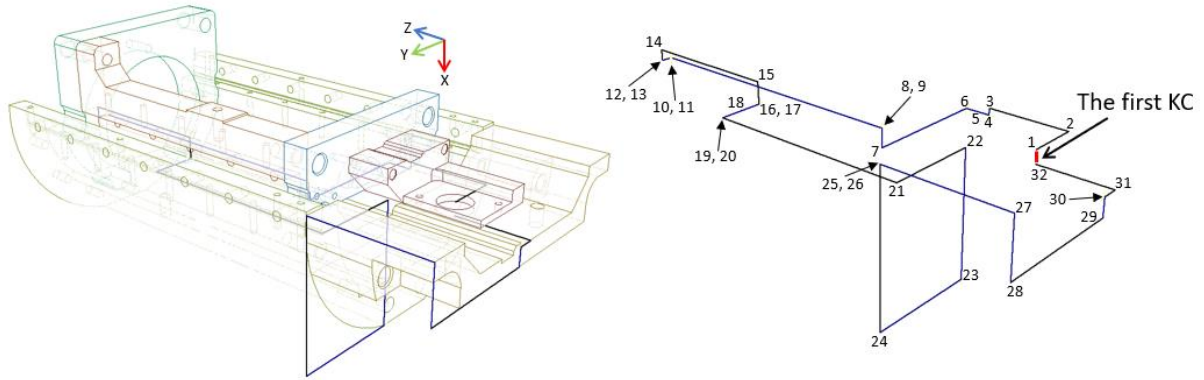
**Figure 14.** Tolerance chain of the first KC.

The first KC is the plane angle deviation between the encoder read head and the measuring scale (see figure 11). This KC is important to ensure that the linear encoder operates within its manufacturer specification (20 nm resolution). The tolerance chain of this KC is shown in figure 14 and is represented as $\mathbf{T_{32}^1}$ that is the transformation of the reference frame from feature #1 to feature #32. The complete tolerance chain of the first KC $\mathbf{T_{32}^1}$ can be calculated as:

$$\mathbf{T_{32}^1} = \mathbf{DT_1\ T_2^1\ DT_2\ T_3^2\ DT_3\ T_4^3\ DT_4\ T_5^4\ DT_5\ T_6^5\ DT_6 T_7^6\ T_8^7\ T_9^8\ DT_9\ T_{10}^9\ DT_{10}\ T_{11}^{10}\ DT_{11}\ T_{12}^{11}\ T_{13}^{12}}$$
$$\mathbf{DT_{13}\ T_{14}^{13}\ DT_{14}\ T_{15}^{14}\ DT_{15}\ T_{16}^{15}\ T_{17}^{16}\ T_{18}^{17}\ DT_{18}\ T_{19}^{18}\ T_{20}^{19}\ DT_{20}\ T_{21}^{20}\ DT_{21} T_{22}^{21}\ DT_{22}\ T_{23}^{22}\ DT_{23}\ T_{24}^{23}}$$
$$\mathbf{T_{25}^{24}\ T_{26}^{25}\ DT_{26}\ T_{27}^{26}\ DT_{27}\ T_{28}^{27}\ T_{29}^{28}\ DT_{29}\ T_{30}^{29}\ DT_{30}\ T_{31}^{30}\ DT_{31}\ T_{32}^{31}}. \tag{3}$$

In an ideal situation, where there are no geometrical variations of the components along the tolerance chain of this first KC, $\mathbf{T_{32}^1}$ is given by:

$$\mathbf{T_{32}^1} = \mathbf{T_2^1\ T_3^2\ T_4^3\ T_5^4\ T_6^5\ T_7^6\ T_8^7\ T_9^8\ T_{10}^9\ T_{11}^{10}\ T_{12}^{11}\ T_{13}^{12}\ T_{14}^{13}\ T_{15}^{14}\ T_{16}^{15}\ T_{17}^{16}\ T_{18}^{17}\ T_{19}^{18}\ T_{20}^{19}\ T_{21}^{20}\ T_{22}^{21}\ T_{23}^{22}\ T_{25}^{24}}$$
$$\mathbf{T_{26}^{25}\ T_{27}^{26}\ T_{28}^{27}\ T_{29}^{28}\ T_{30}^{29}\ T_{31}^{30}\ T_{32}^{31}} \tag{4}$$

where

$$T_{32}^1 = \begin{bmatrix} 1 & 0 & 0 & 3575 \\ 0 & 1 & 0 & 0 \\ 0 & 0 & 1 & 0 \\ 0 & 0 & 0 & 1 \end{bmatrix}. \tag{5}$$

From the calculation of the chain of the transformation, the distance and parallelism of the first KC are 3575 μm along the *x*-axis direction and 0 μm, respectively.
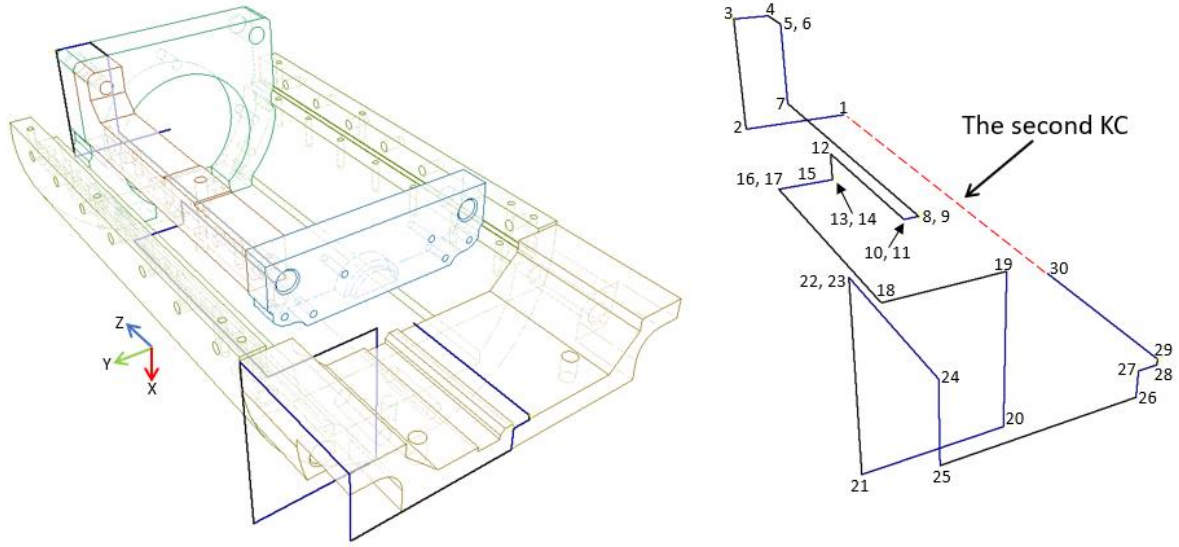
**Figure 15.** Tolerance chain of the second KC.

The second KC is the axis deviation between the optical system and the measuring scale axes (see figure 12). This KC controls the quantity of the parasitic rotation between the optical system and the measuring scale axis. Figure 15 shows the tolerance chain of the second KC that is represented as $\mathbf{T_{30}^1}$. The complete tolerance chain $\mathbf{T_{30}^1}$ can be expressed as:

$$\mathbf{T_{30}^1 = DT_1\ T_2^1\ DT_2\ T_3^2\ DT_3\ T_4^3\ T_5^4\ DT_5\ T_6^5\ DT_6\ T_7^6\ DT_7\ T_8^7\ T_9^8\ DT_9\ T_{10}^9\ T_{11}^{10}\ DT_{11}T_{12}^{11}\ DT_{12}\ T_{13}^{12}}$$
$$\mathbf{DT_{13}\ T_{14}^{13}\ T_{15}^{14}\ DT_{15}\ T_{16}^{15}\ T_{17}^{16}\ DT_{17}\ T_{18}^{17}\ DT_{18}\ T_{19}^{18}\ DT_{19}\ T_{20}^{19}\ DT_{20}\ T_{21}^{20}\ T_{22}^{21}\ T_{23}^{22}\ DT_{23}\ T_{24}^{23}\ DT_{24}}$$
$$\mathbf{T_{25}^{24}\ T_{26}^{25}\ DT_{26}\ T_{27}^{26}\ DT_{27}\ T_{28}^{27}\ DT_{28}\ T_{29}^{28}\ T_{30}^{29}}.\qquad(6)$$

Calculated in a similar way as for the first KC, in an ideal situation, where there are no geometrical variations of the components along the tolerance chain of this first KC, $\mathbf{T_{30}^1}$ is given by:

$$T_{30}^1 = \begin{bmatrix} 1 & 0 & 0 & 0 \\ 0 & 1 & 0 & 0 \\ 0 & 0 & 1 & -104000 \\ 0 & 0 & 0 & 1 \end{bmatrix}. \qquad (7)$$

From the calculation of the chain of the transformation, the distance and axis deviation of the second KC are 104,000 μm along the z-axis direction and 0°, respectively.

*4.2 Simulation results of the tolerance stack-ups of the two KCs*

Based on the specified tolerances for all parts that contribute to the KCs, simulations of the tolerance stack-ups of both KCs have been performed in MATLAB. Both simulations run with 50,000 iterations and the random variables of the geometric error of the features are assumed to be normally distributed. The values assigned to the nominal matrix $\mathbf{T_j^i}$ and the variation matrix $\mathbf{DT_i}$ for the tolerance chains of both KCs are presented in Appendix 1.

The results of the tolerance stack-up variations for the first and the second KCs are shown in figure 16 and figure 17, respectively. For the first KC, the distance variation between the planes of the

mounted reading head and linear encoder is ±150 μm along the *x*-axis direction and is within the specification of the linear encoder assembly from the manufacturer. The plane angle deviation can be derived from the combination of angle variations from the rotation about *x*-, *y*- and *z*-axes; they are ±0.5°, ±0.12° and ±0.04° respectively. Similarly, for the second KC, the Abbe offset variation in *x*- and *y*-axes between the optical system datum and the linear scale datum are ±140 μm and ±350 μm respectively. The axis deviation for the second KC can be derived from the combination of angle variations from the rotation about *x*- and *y*-axes; they are ±0.5° and ±0.11° respectively.
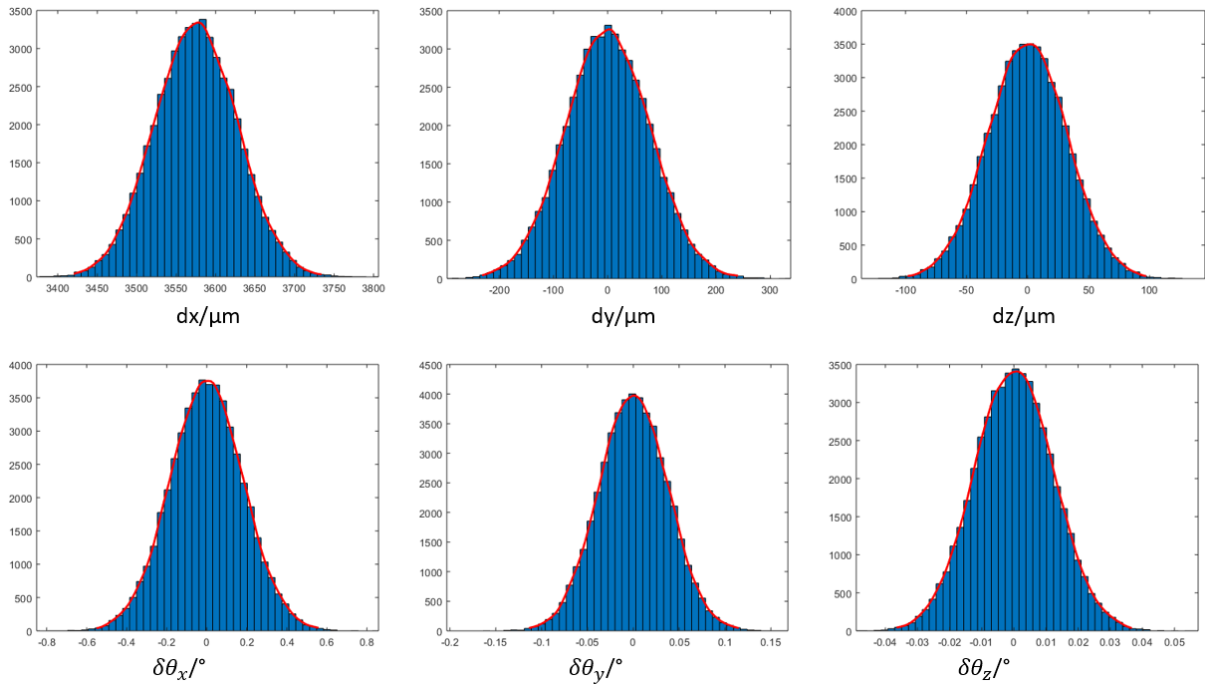


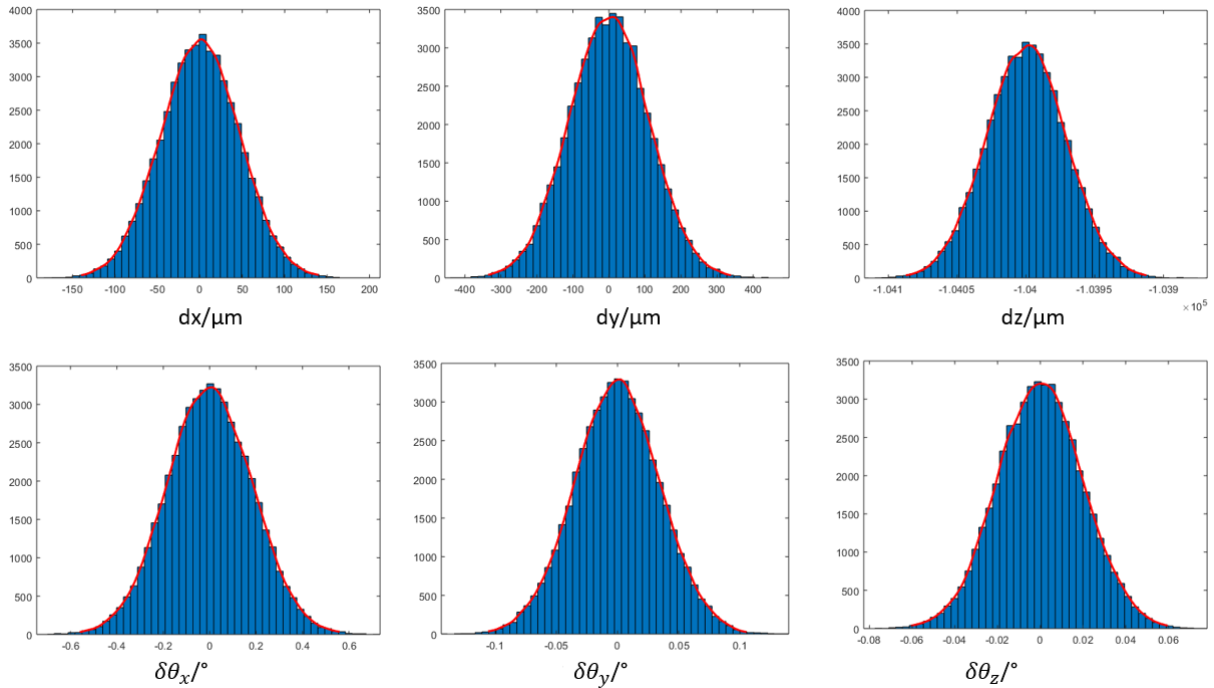**Figure 16.** Simulation result for the first KC.

**Figure 17.** Simulation result for the second KC.

### 4.3 Verification of the two KCs deviations

From the tolerance stack-up analyses, the deviation of translation and rotational components with respect to the ideal defined KCs can be associated to the part features (for example, planes and simple geometric shapes). With a tactile CMM, the KC features can be measured and compared with the simulation results. The strategies for the CMM measurements were defined to enable the reconstruction of geometrical features to calculate the KCs. The calculation procedure to obtain the plane angle deviation of the first KC and the axis deviation of the second KC are:

- The plane angle deviation of the first KC is derived by measuring two planes representing the surface on which the reading head and the linear encoder scale are mounted (see figure 18). From the measured planes, their angle with respect to the reference coordinate system is calculated. The differences in their measured angle represent the deviation between the planes on which the reading head and the linear encoder scale are mounted.

- A coordinate frame (reference) is established by measuring the four planes on part 1 (see figure 19). The deviation of the optical axis with respect to a coordinate frame (reference) is derived from the part 2 plane feature (see figure 19), where the optical system is mounted. From the measured plane, the measured angle with respect to the coordinate frame represents the deviation.
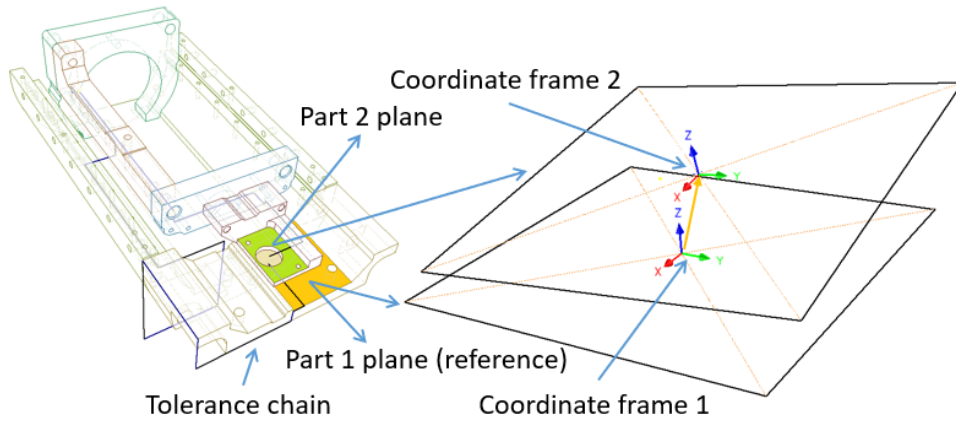
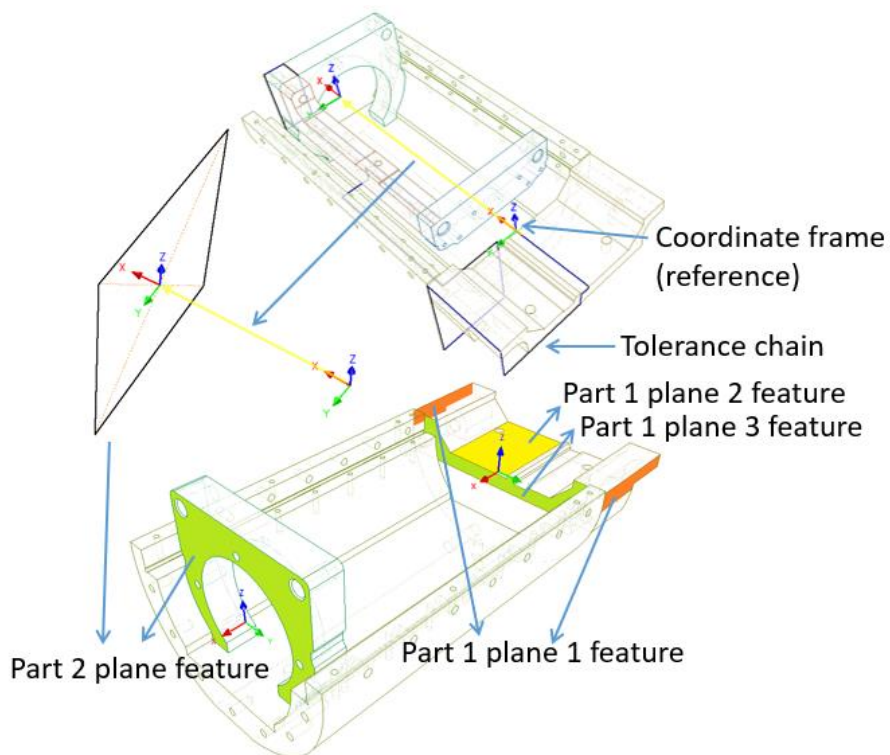**Figure 18.** The CMM calculation procedure for the first KC.



**Figure 19.** The CMM calculation procedure for the second KC.

**Figure 20.** CMM measurements for the verification of the KCs.

**Table 1.** The two KC variation values from the assembly, measured using a CMM.

| Measurements | First KC | | | Second KC | | |
|:---:|:---:|:---:|:---:|:---:|:---:|:---:|
| | $d\theta x/°$ | $d\theta y/°$ | $d\theta z/°$ | $d\theta x/°$ | $d\theta y/°$ | $d\theta z/°$ |
| 1 | -0.154 | -0.011 | 0.128 | 0.01 | -0.039 | -0.041 |
| 2 | -0.171 | -0.021 | 0.144 | 0.011 | -0.039 | -0.041 |
| 3 | -0.151 | -0.017 | 0.125 | 0.017 | -0.031 | -0.035 |
| 4 | -0.154 | -0.018 | 0.127 | 0.007 | -0.04 | -0.041 |
| 5 | -0.162 | -0.013 | 0.136 | 0.012 | -0.039 | -0.041 |

       Figure 20 shows the CMM measurement strategies for the verification of two KCs' deviations. From the CMM measurement results, adjustment of the reference coordinate system of CMM with respect to the reference coordinate system of the simulations is required. Table 1 shows that the two KC variation values from CMM measurement results can be compared with the simulation results. These comparisons are shown in figure 21 and 22; the rotational component deviations from simulation results are stacked with the yellow line as the approximate value of the rotational component deviations from CMM measurements. Only the rotational component of the *z*-axis of the first KC is outside the simulation range. This could be caused by of the variation in the assembly for the part on which the encoder read head is mounted. Although the rotational deviation along the *z*-axis is out of the tolerance prediction, the linear encoder can still perform to its specification because the rotational deviation is within the tolerance given by the linear encoder manufacturer. In addition, the *z*-axis is along the optical axis so that the rotational error about the *z*-axis will not affect the measurement accuracy, which is highly dependent on the accuracy of the linear translation along the *z*-axis.
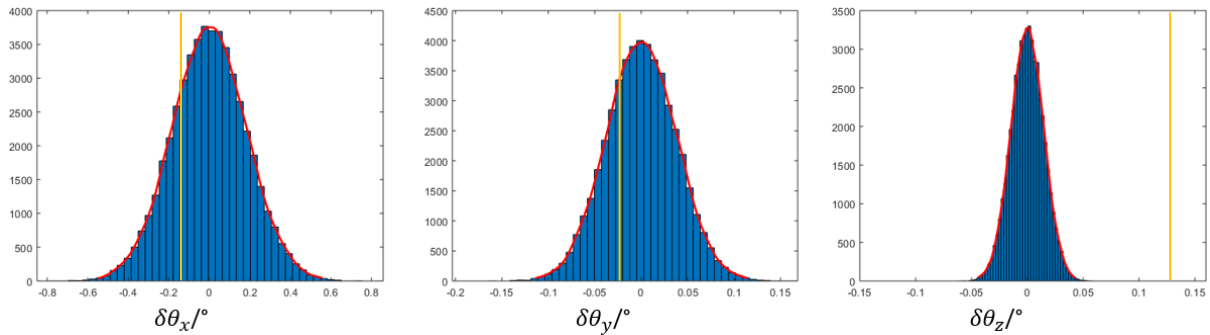
**Figure 21.** Comparison between the simulation and CMM measurements of the first KC. The yellow line indicates the approximate rotational values from the CMM measurements.
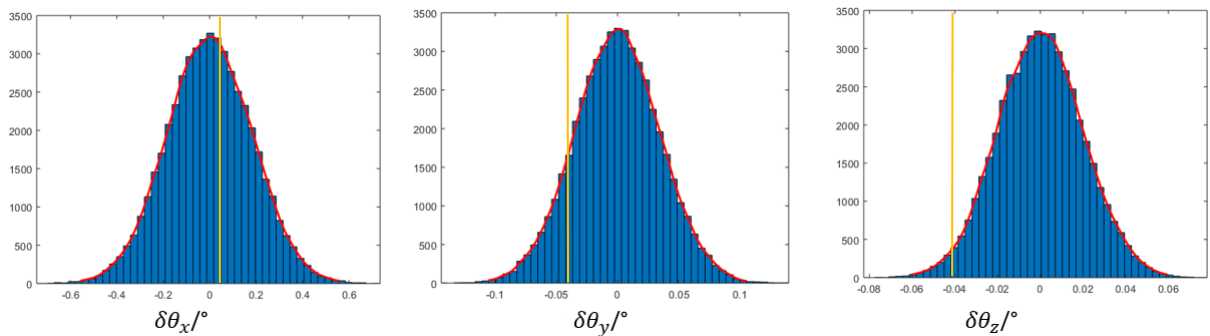


**Figure 22.** Comparison between the simulation and CMM measurements of the second KC. The yellow line indicates the approximate rotational values from the CMM measurements.

## 5. Linear motion accuracy verification

To verify the accuracy of the motion stage of the sensor, a Renishaw XL-80 laser interferometer was used to measure the linear, pitch and yaw errors. The experimental setup is shown in figure 23. The laser interferometer is equipped with an environmental compensator (Renishaw XC-80) to minimise and adjust the measurement error associated with the variation in air temperature, air pressure and relative humidity [48]. The interferometer setup for the linear or angular measurements uses retroreflectors that are mounted on to the carriage or the moving part of the sensor (see figure 23). The apex axis of the retroreflectors is approximately in-line with the optical axis, reducing the cosine error during measurement.

Figure 24 is a schema of the interferometer setup for both linear and angular displacement measurements. Referring to figure 24, a laser beam is emitted from the source and split into a reference beam and a measurement beam by a beam-splitter. The reflected beams of the measurement and reference paths are combined and detected.
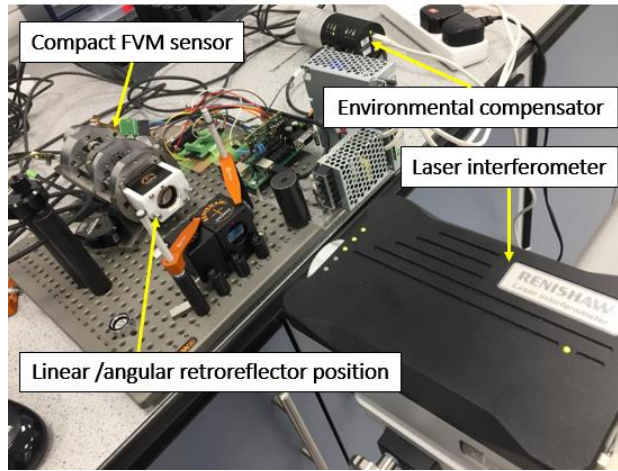
**Figure 23.** Laser interferometer measurement setup.
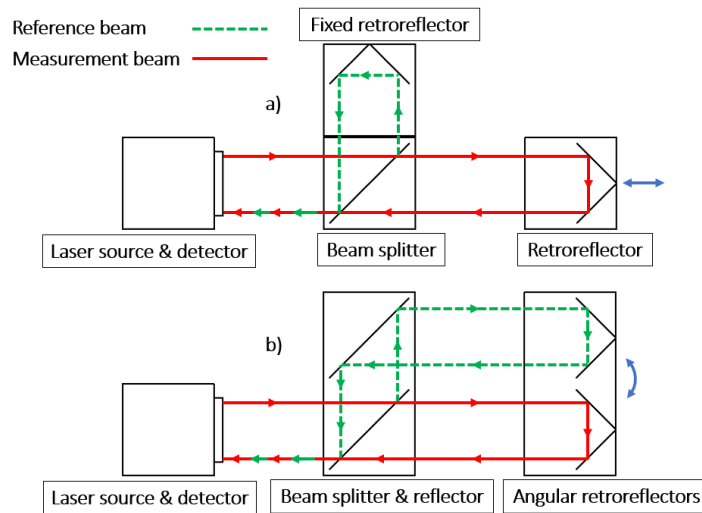


**Figure 24.** a). Laser interferometer optical setup for linear measurement. (b). Setup for angular measurement.

**Table 2.** Uncertainty budget for the linear measurement using the laser interferometer.

| Quantity | Estimated or measured value | Standard uncertainty | Sensitivity coefficient | Contribution to standard uncertainty in P20 (µm) |
|---|---|---|---|---|
| $X_i$ | $x_i$ | $u_i$ | $c_i = \dfrac{\partial P_{20}}{\partial X_i}$ | $= c_i u_i$ |
| $L_{nominal}$ | 20 mm | | | |
| $L_{20}$ | 20000.176 mm | 0.27 µm | 1 | 0.27 |
| $\alpha_s$ | $8\times10^{-6}$ °C$^{-1}$ | $8\times10^{-7}$ °C$^{-1}$ | 22000.194 µm°C | 0.018 |
| $T_s$ | 21.1 °C | 0.2 °C | 0.16 µm/°C | 0.032 |

| | | | | |
|---|---|---|---|---|
| $T_a$ | 20.7 °C | 0.4 °C | 0.0192 µm/°C | 0.008 |
| $P_a$ | 1019 hPa | 2 hPa | 0.0054 µm/hPa | 0.011 |
| $H$ | 47 %RH | 12 %RH | 0.002 µm/%RH | 0.024 |

$$u(L_{1,x}) = \sqrt{\sum(u_i c_i)^2} \qquad 0.27$$

The laser interferometer measurements were performed for both forward and backward movements so that the hysteresis of the motion was considered. Each measurement was repeated five times for 20 mm travel with 1 mm intervals. From the measurements, the maximum linear error in both directions was less than 2 µm (see figure 25). A systematic linear slope trend was evident in the measurement data that could be compensated in the controller. The overall pitch and yaw errors in both directions were less than 30 µrad (see figure 26 and 27). The calibration expanded uncertainty ($k = 2.17$, obtained from the Welch-Satterthwaite formula with degree of freedom of 14) for the maximum 20 mm length measurement is 0.59 µm (see table 2).



(a)                                      (b)

**Figure 25.** Linear position errors for forward (a) and backward (b).



(a)                                      (b)

**Figure 26.** Pitch errors for forward (a) and backward (b).
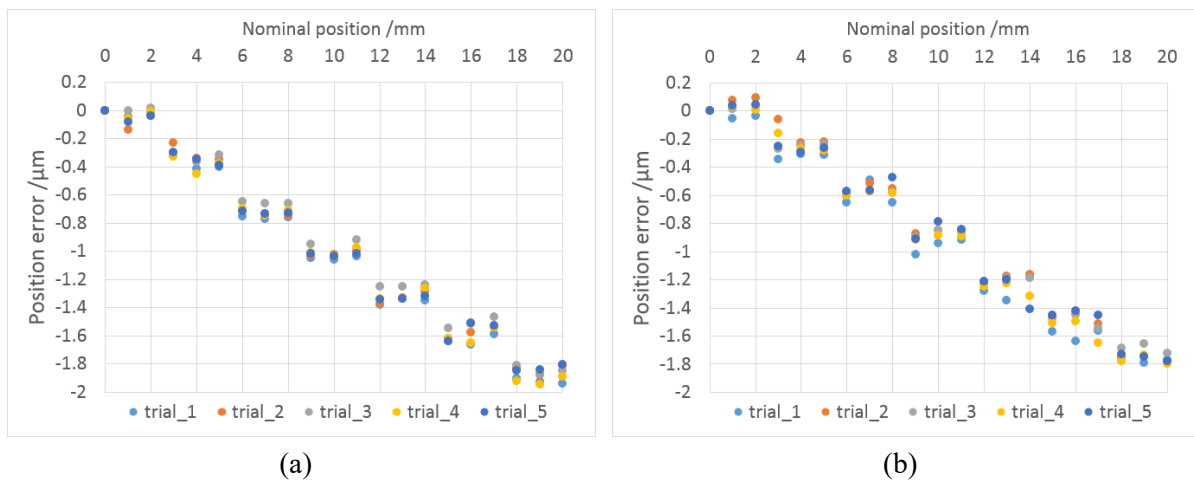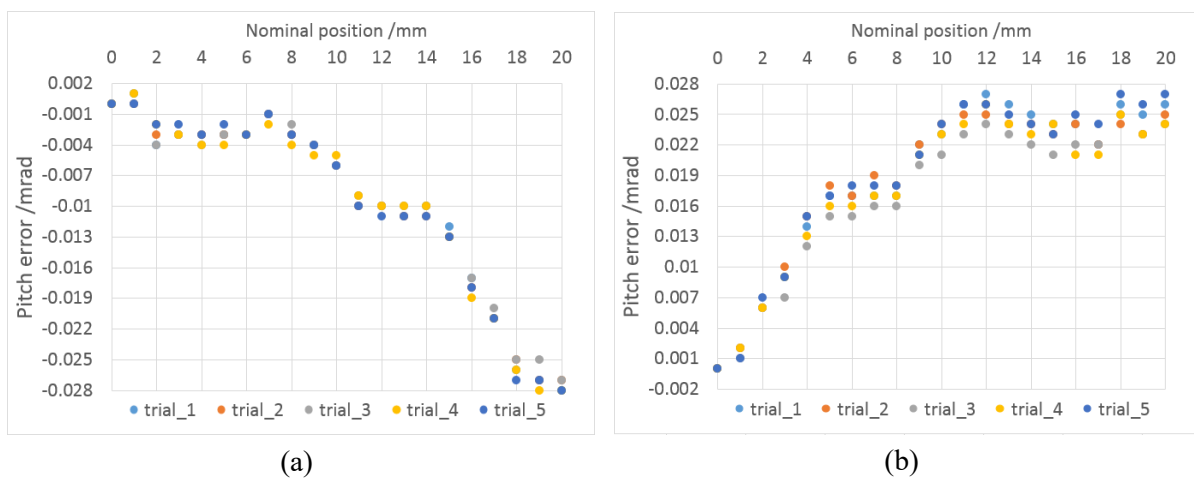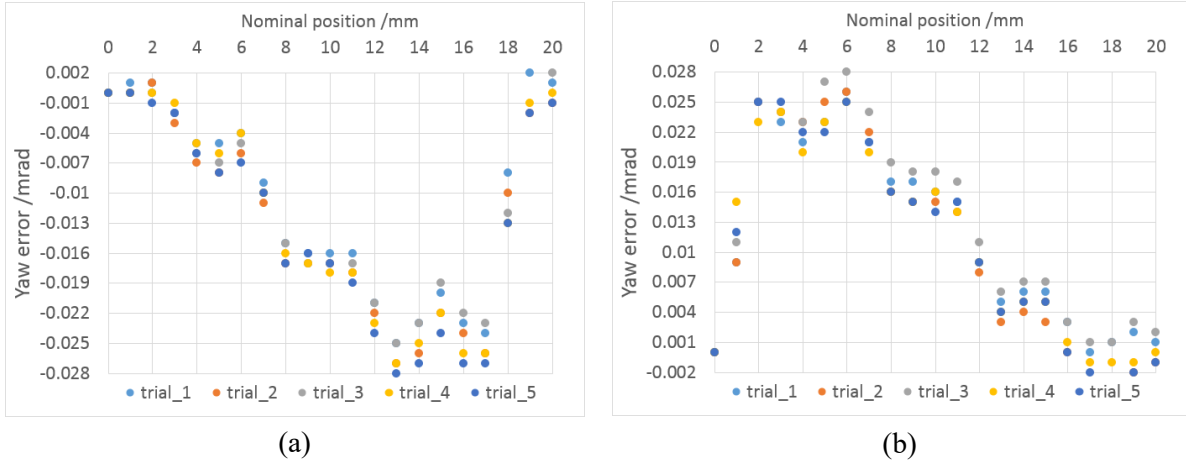
**Figure 27.** Yaw errors for forward (a) and backward (b).

## 6. Measurement of a calibrated artefact

The step height measurement capability and the measurement noise of the compact FVM sensor were computed from the measurement of a flat region on a step height artefact (Alicona IF-Calibration Tool). From the top plane of the step height, a flat area of (0.75 × 0.75) mm was measured three times, then evaluated by applying a subtraction method to compute the measurement noise [49]. The measurement was performed in a controlled laboratory at 20 °C ± 0.5 °C. For comparison, an identical procedure was applied for an off-line FVM. Table 3 shows the measurement noise of the compact FVM sensor and the off-line FVM and a difference can be observed. This difference is associated with the low-cost prototype optical system and noise during the scanning of the motion stage.

**Table 3.** Measurement noise comparison with 10× magnification objective lens.

| Subtractions | Compact FVM sensor | Off-line FVM |
|:---:|:---:|:---:|
| | $Sq_{noise}/\mu m$ | $Sq_{noise}/\mu m$ |
| 1 | 0.373 | 0.145 |
| 2 | 0.389 | 0.159 |
| 3 | 0.391 | 0.154 |

Step height measurements of the calibrated artefact were also conducted three times (see table 4). The calibrated height was 0.99999 mm ± 0.00001 mm. The measured step height area was (1 × 1) mm as shown in figure 28a. For the step height plane measurements, after a surface levelling procedure with respect to the top plane, the bottom plane was defined as a datum. To fit two parallel planes, a least-squares method was applied. The distance between the two parallel planes was calculated as the depth as shown in figure 28b. From figure 28b, the average error of the height measurement with respect to the calibrated value is 0.3 μm.

**Table 4.** Step height measurements.

| Measurements | Step height/mm |
|:---:|:---:|
| 1 | 0.9993 |
| 2 | 0.9991 |
| 3 | 0.9994 |

**Figure 28.** (a) Step height measurement by the compact FVM sensor. (b) Measured step height profile.

## 7. Conclusions

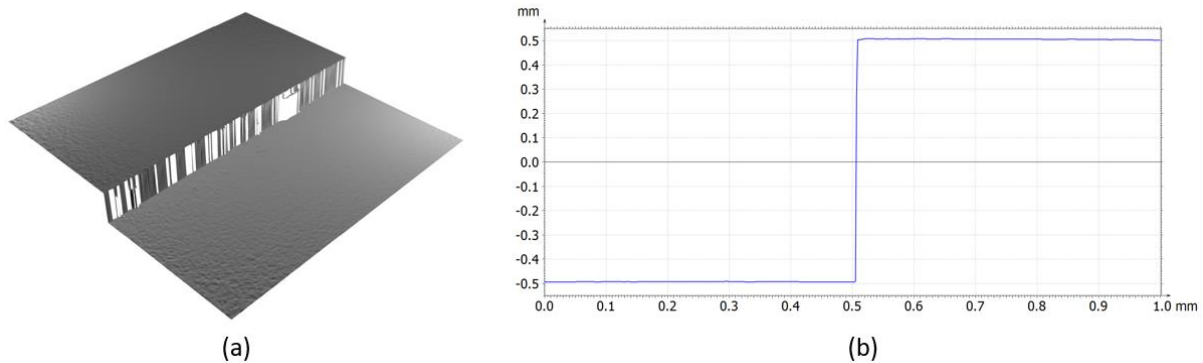A compact FVM sensor has been developed and its performance verified. This sensor can perform surface topography measurements in the chamber of different types of machine tools. The sensor's design complies with the Abbe principle for the configuration of the linear encoder and the optical system. The geometry of the sensor is cylindrical with 78 mm diameter and 200 mm height. The maximum linear motion of the sensor is 20 mm.

FEA simulations are performed to evaluate the mechanical deformation and vibration properties of the structure of the sensor. From the simulations, the results show that the deformation of the structure due to temperature increases are within the desired specification. To analyse the geometrical variation of the sensor assembly, tolerance stack-up chain simulations were performed. From this analysis, the allocated geometrical and dimensional tolerance of the parts of the sensor can be optimised to meet manufacturing requirements and achieve the allowable variation limit that assures the parts can function properly. In addition, by measuring the sensor assembly using a CMM, the rotational components of the defined KCs between the simulations and the assembly can be compared. The comparison shows that only the rotational component of the $z$-axis from the first KC is outside the simulation range and could be due to assembly errors.

The linear motion characteristics of the sensor were measured with a laser interferometer. The maximum linear motion error was 2 μm and 30 mrad for angular error for the full 20 mm motion. The mean result for the measurement noise for the sensor was 0.384 μm and the dimensional measurement accuracy of the sensor shows a measurement error of less than 1 μm. Both measurements were performed in a controlled environment and a step-height artefact was used for the measurements.

The novelty of the development is the compact design solution for a small-size on-machine FVM sensor which will ease the integration of the sensor within the chamber of different types of machine tools and articulated or collaborative robots. The design of the sensor is mainly constrained by the required overall maximum dimensions of common machine tool changer magazines. The sensor can be used for generic on-machine measurement in machine tools. A case study, in order to evaluate the feasibility of the sensor, involving the on-machine dimensional measurement of the depth of hydrophobic microscale features (including the geometry of microchannels and micro-dimples, and surface texture) is presented elsewhere [50].

Future work will focus on the development of an integrated wifi solution within the compact FVM sensor, optimisation of the optical system, a robust enclosure that protects the sensor from contaminants, such as oil and debris, and the full integration of compact FVM sensor into a commercial machine tool.

**References**

1. Colledani M, Tolio T, Fischer A, Iung B, Lanza G, Schmitt R and Váncza J 2014 Design and management of manufacturing systems for production quality *Ann. CIRP* **63** 773-796
2. Gao W, Haitjema H, Fang FZ, Leach RK, Cheung CF, Savio E and Linares JM 2019 On-machine and in-process surface metrology for precision manufacturing *Ann. CIRP* **68** 843-866
3. Syam WP, Rybalcenko K, Gaio A, Crabtree J and Leach RK 2019 Methodology for the development of in-line optical surface measuring instruments with a case study for additive surface finishing *Opt. Lasers Eng.* **121** 271-288
4. Syam WP 2020 In-process surface topography measurements. In: Leach RK *Advances in Optical Surface Texture Metrology* (IOP Publishing)
5. Uhlmann E, Mullany B, Biermann D, Rajurkar KP, Hausotte T and Brinksmeier E 2016 Process chains for high-precision components with micro-scale features *Ann. CIRP* **65** 549-572
6. Graves LR, Smith GA, Apai D and Kim DW 2019 Precision optics manufacturing and control for next-generation large telescopes *Nanomanufacturing and Metrology* **2** 65-90
7. Chen YL, Niu Z, Matsuura D, Lee JC, Shimizu Y, Gao W, Oh JS and Park CH 2017 Implementation and verification of a four-probe motion error measurement system for a large-scale roll lathe used in hybrid manufacturing *Meas. Sci. Technol.* **28** 105004
8. Li D, Cheung CF, Ren M, Whitehouse D and Zhao X 2015 Disparity pattern-based autostereoscopic 3D metrology system for in situ measurement of microstructured surfaces *Opt. Lett.* **40** 5271-5274
9. Zou X, Zhao X, Li G, Li Z and Sun T 2017 Non-contact on-machine measurement using a chromatic confocal probe for an ultra-precision turning machine *Int. J. Adv. Manuf. Technol.* **90** 2163-2172
10. Li D, Jiang X, Tong Z and Blunt L 2019 Development and application of interferometric on-machine surface measurement for ultraprecision turning process *ASME – J. Manuf. Sci. Eng.* **14** 014502
11. Syam WP, Jianwei W, Zhao B, Maskery I, Elmadih W, Leach R 2018 Design and analysis of strut-based lattice structures for vibration isolation *Prec. Eng.* **52** 494–506
12. Elmadih W, Syam WP, Maskery I, Chronopoulos D, Leach R 2019 Mechanical vibration bandgaps in surface-based lattices *Additive Manufacturing* **25** 421–429
13. Muhamedsalih H, Jiang X, Gao F 2010 Vibration compensation of wavelength scanning interferometer for in-process surface inspection *The 10th Proceedings of Computing and Engineering Annual Researchers' Conference 2010* 148–153
14. Schmitt R, Peterek M 2015 Traceable measurements on machine tools - Thermal influences on machine tool structure and measurement uncertainty *Procedia CIRP* **33** 576–580
15. Berger D, Brabandt D, Lanza G 2015 Conception of a mobile climate simulation chamber for the investigation of the influences of harsh shop floor conditions on in-process measurement systems in machine tools *Measurement* **74** 233–237
16. Acko B, Klobucar R, Acko M 2015 Traceability of in-process measurement of workpiece geometry *Procedia Engineering* **100** 376–383

17. Li D, Tong Z, Xiang J, Blunt L, Gao F 2018 Calibration of an interferometric on-machine probing system on an ultra-precision turning machine *Measurement* **118** 96–104

18. Zangl K, Danzl R, Helmli F and Prantl M 2018 Highly accurate optical μCMM for measurement of micro holes *Proc. CIRP* **75** 397-402

19. Repitsch C, Zangl K, Helmli F, Danzl R 2020 Focus variation. In: Leach RK *Advances in Optical Surface Texture Metrology* (IOP Publishing)

20. Demir AG, Previtali B 2017 Additive manufacturing of cardiovascular CoCr stents by selective laser melting *Mater. Des.* **119** 338-350

21. Newton L, Senin N, Gomez C, Danzl R, Helmli F, Blunt L, Leach R 2019 Areal topography measurement of metal additive surfaces using focus variation microscopy *Addit. Manuf.* **25** 365-389

22. Wang P, Sin WJ, Nai MLS, Wei J 2017 Effects of processing parameters on surface roughness of additive manufactured Ti-6Al-4V via electron beam melting *Materials* **10** 8–14 https://doi.org/10.3390/ma10101121

23. Rosa B, Mognol P, Hascoet J-Y 2015 Laser polishing of additive laser manufacturing surfaces, *J. Laser Appl.* **27** https://doi.org/10.2351/1.4906385

24. Triantaphyllou A, Giusca CL, Macaulay GD, Roerig F, Hoebel M, Leach RK, Tomita B, Milne KA 2015 Surface texture measurement for additive manufacturing *Surf. Topogr. Metrol. Prop.* **3** 024002 https://doi.org/10.1088/2051-672X/3/2/024002

25. Cabanettes F, Joubert A, Chardon G, Dumas V, Rech J, Grosjean C, Dimkovski Z 2018 Topography of as built surfaces generated in metal additive manufacturing: a multi scale analysis from form to roughness *Precis. Eng.* **52** 249–265

26. Walton K, Blunt L, Fleming L, Goodhand M, Lung H 2014 Areal parametric characterisation of ex-service compressor blade leading edges *Wear* **321** 79-86

27. Zhang X, Tnay GL, Liu K, Kumar AS 2018 Effect of apex offset inconsistency on hole straightness deviation in deep hole gun drilling of Inconel 718 *Int. J. Mach. Tool. Manuf.* **125** 123-132

28. Nasrollahi V, Penchev P, Dimov S, Korner L, Leach R, Kim K 2017 Two-Side Laser Processing Method for Producing High Aspect Ratio Microholes *Journal of Micro Nano-manufacturing* **5**(4) 041006

29. Danzl R, Lankmair T, Calvez A, Helmli F 2017 Robot solutions for automated 3D surface measurement in production *18th International Congress of Metrology 2017* 15002

30. Darukumalli S, Santoso T, Syam WP, Helmli F and Leach RK 2019 On-machine optical surface topography measurement sensor based on focus variation *Proc. 19th Int. euspen Conf., Bilbao, Spain, June* 182-185

31. Altintas Y, Verl A, Brecher C, Uriarte L, and Pritschow G 2019 Machine tool feed drives *Ann. CIRP* **60** 779-796

32. Ruijl T Ultra-precision coordinate measuring machine In: PhD thesis. Delft University of Technology; 2001

33. Bos E, Moers T, and van Riel M 2015 Design and verification of an ultra-precision 3D-coordinate measuring machine with parallel drives *Meas. Sci. Technol.* **26** 085904

34. Smith ST 2018 Precision machine principles and elements. In: Leach RK, Smith ST *Basics of Precision Engineering* (CRC Press)

35. Ramesh R, Mannan M, and Poo A 2000 Error compensation in machine tools – a review: Part I: Geometric, cutting-force induced and fixture-dependent errors *Int. J. Adv. Manuf. Technol.* **40** 1235–1256

36. Brecher C, Utsch P, and Wenzel C 2009 Five-axes accuracy enhancement by compact and integral design *Ann. CIRP* **58** 355–358

37. Bosmans N, Qian J, and Reynaerts D 2017 Design and experimental validation of an ultra-precision Abbe-compliant linear encoder-based position measurement system *Prec. Eng.* **47** 197-211

38. Slocum AH 1992 *Precision Machine Design* (Society of Manufacturing Engineers)
39. Schellekens P, Rosielle N, Vermeulen H, Vermeulen M, Wetzels S, Pril W 1998 Design for precision: current status and trends *Ann. CIRP* **47** 557–586
40. Schwenke H, Knapp W, Haitjema H, Weckenmann A, Schmitt R, and Delbressine F 2008 Geometric error measurement and compensation of machines – an update *Ann. CIRP* **57** 660–675
41. Mayr J, Jedrzejewski J, Uhlmann E, Donmez MA, Knapp W, and Haertig F 2012 Thermal issues in machine tools *Ann. CIRP* **61** 771–791
42. Leach RK 2020 Integrated metrology 10-year roadmap for advanced manufacturing (HVM Catapult)
43. Helmli F 2011 Focus variation instruments. In: Leach RK *Optical Measurement of Surface Topography* (Springer)
44. Whitney DE 2004 *Mechanical Assemblies: Their Design, Manufacture, and Role in Product Development* (USA: Oxford University Press)
45. Elmadih W, Nefzi M, Buice ES 2018 Environmental isolation. In: Leach RK, Smith ST *Basics of Precision Engineering* (CRC Press)
46. Hedderich J Thermal stability in machine tools In: Master thesis. Royal Institute of Technology; 2015
47. Seugling R 2018 System modelling. In: Leach RK, Smith ST *Basics of Precision Engineering* (CRC Press)
48. Haitjema H 2008 Achieving traceability and sub-nanometer uncertainty using interferometric techniques *Meas. Sci. Technol.* **19** 084002
49. Giusca CL, Leach RK, Helary F, Gutauskas T and Nimishakavi L 2012 Calibration of the scales of areal surface topography-measuring instruments: part 1. Measurement noise and residual flatness *Meas. Sci. Technol.* **23** 035008
50. Santoso T, Syam WP, Darukumalli S, Cai Y, Helmli F, Luo X and Leach RK 2020 On-machine focus variation measurement for micro-scale hybrid surface texture machining *Int. J. Adv. Manuf. Technol.* **109** 2353–2364

## Appendix 1

Note that the values in table 5 to table 8 are the results from one iteration out of 50,000 iterations.

**Table 5.** Nominal tolerance chain of the first KC.

| Chain | Description | Roto-translation matrix | | | | | |
| | | Translation | | | Rotation | | |
| | | $d_x/\mu m$ | $d_y/\mu m$ | $d_z/\mu m$ | $d\theta_x/°$ | $d\theta_y/°$ | $d\theta_z/°$ |
|---|---|---|---|---|---|---|---|
| 1-2 | Nominal dimension + tolerance | 0 | 13849.4 | 0 | 0 | 0 | 0 |
| 2-3 | Nominal dimension + tolerance | 0 | 0 | 22750.4 | 0 | 0 | 0 |
| 3-4 | Nominal dimension + tolerance | 1849.7 | 0 | 0 | 0 | 0 | 0 |
| 4-5 | Nominal dimension + tolerance | 0 | 0 | 0 | 0 | 0 | 0 |
| 5-6 | Nominal dimension + tolerance | 0 | 0 | 7000.6 | 0 | 0 | 0 |
| 6-7 | Nominal dimension + tolerance | | 32581.0 | 0 | 0 | 0 | 0 |
| 7-8 | Nominal dimension + tolerance | 4875.1 | 0 | 0 | 0 | 0 | 0 |
| 8-9 | Nominal dimension + tolerance | 0 | 0 | 0 | 0 | 0 | 0 |

| | | | | | | | |
|---|---|---|---|---|---|---|---|
| 9-10 | Nominal dimension + tolerance | 0 | 0 | 77000.4 | 0 | 0 | 0 |
| 10-11 | Nominal dimension + tolerance | 0 | 0 | 0 | 0 | 0 | 0 |
| 11-12 | Nominal dimension + tolerance | 0 | 3000.4 | 0 | 0 | 0 | 0 |
| 12-13 | Nominal dimension + tolerance | 0 | 0 | 0 | 0 | 0 | 0 |
| 13-14 | Nominal dimension + tolerance | 2999.6 | 0 | 0 | 0 | 0 | 0 |
| 14-15 | Nominal dimension + tolerance | 0 | 0 | 38499.5 | 0 | 0 | 0 |
| 15-16 | Nominal dimension + tolerance | 6000.2 | 0 | 0 | 0 | 0 | 0 |
| 16-17 | Nominal dimension + tolerance | 0 | 0 | 0 | 0 | 0 | 0 |
| 17-18 | Nominal dimension + tolerance | 0 | 5999.3 | 0 | 0 | 0 | 0 |
| 18-19 | Nominal dimension + tolerance | 0 | 5999.8 | 0 | 0 | 0 | 0 |
| 19-20 | Nominal dimension + tolerance | 0 | 0 | 0 | 0 | 0 | 0 |
| 20-21 | Nominal dimension + tolerance | 0 | 0 | 55498.8 | 0 | 0 | 0 |
| 21-22 | Nominal dimension + tolerance | 0 | 24281.3 | 0 | 0 | 0 | 0 |
| 22-23 | Nominal dimension + tolerance | 34500.5 | 0 | 0 | 0 | 0 | 0 |
| 23-24 | Nominal dimension + tolerance | 0 | 29650.2 | 0 | 0 | 0 | 0 |
| 24-25 | Nominal dimension + tolerance | 40686.1 | 0 | 0 | 0 | 0 | 0 |
| 25-26 | Nominal dimension + tolerance | 0 | 0 | 0 | 0 | 0 | 0 |
| 26-27 | Nominal dimension + tolerance | 0 | 0 | 32999.9 | 0 | 0 | 0 |
| 27-28 | Nominal dimension + tolerance | 14812.1 | 0 | 0 | 0 | 0 | 0 |
| 28-29 | Nominal dimension + tolerance | 0 | 34718.5 | 0 | 0 | 0 | 0 |
| 29-30 | Nominal dimension + tolerance | 5025.7 | 0.000 | 0 | 0 | 0 | 0 |
| 30-31 | Nominal dimension + tolerance | 0 | 4380.4 | 0 | 0 | 0 | 0 |
| 31-32 | Nominal dimension + tolerance | 0 | 0 | 20249.8 | 0 | 0 | 0 |

**Table 6.** Variation tolerance chain of the first KC.

| Chain | Description | matriks Roto-translation matrix | | | | | |
|---|---|---|---|---|---|---|---|
| | | Translation | | | Rotation | | |
| | | $d_x/\mu m$ | $d_y/\mu m$ | $d_z/\mu m$ | $d\theta_x/°$ | $d\theta_y/°$ | $d\theta_z/°$ |
| 1' | Perpendicularity + dimensional tolerances | 6.49 | 0 | 0 | 0 | -0.02217 | -0.01600 |
| 2' | Perpendicularity + dimensional tolerances | 0 | 1.54 | 0 | -0.00509 | 0 | 0.00093 |
| 3' | Perpendicularity + dimensional tolerances | 0 | 0 | 1.67 | 0.00812 | 0.00280 | 0 |
| 4' | Flatness + dimensional tolerances | 0.25 | 0 | 0 | 0 | -0.00587 | 0 |
| 5' | Perpendicularity + dimensional tolerances | 0 | 0 | -0.11 | 0.01172 | 0.00037 | 0 |
| 6' | Flatness + dimensional tolerances | 0 | 0 | -1.76 | 0.00142 | 0.00320 | 0 |
| 9' | Perpendicularity + dimensional tolerances | 0 | 0 | -0.14 | -0.00991 | 0.01857 | 0 |
| 10' | Flatness + dimensional tolerances | 0 | -0.17 | 0.00 | -0.00232 | 0 | 0.00269 |
| 11' | Flatness + dimensional tolerances | 0 | 0 | -2.49 | 0.00290 | 0.00901 | 0 |

| | | | | | | | |
|---|---|---|---|---|---|---|---|
| 13' | Perpendicularity + dimensional tolerances | 0 | 0 | 3.24 | -0.00936 | -0.02210 | 0 |
| 14' | Perpendicularity + dimensional tolerances | 0 | -0.99 | 0 | 0.02655 | 0 | -0.00113 |
| 15' | Perpendicularity + dimensional tolerances | -0.47 | 0 | 0 | 0 | -0.00847 | -0.00041 |
| 18' | Perpendicularity + dimensional tolerances | 0 | -1.87 | 0 | 0.02406 | 0 | 0.00218 |
| 20' | Perpendicularity + dimensional tolerances | 0 | 0.20 | 0 | -0.03102 | 0 | 0.00031 |
| 21' | Perpendicularity + dimensional tolerances | -1.26 | 0 | 0 | 0 | 0.02152 | 0.00099 |
| 22' | Perpendicularity + dimensional tolerances | 0 | 0 | 0.77 | -0.00218 | -0.00060 | 0 |
| 23' | Flatness + dimensional tolerances | -0.52 | 0 | 0 | 0 | -0.00030 | -0.00160 |
| 26' | Perpendicularity + dimensional tolerances | 0 | 0 | 0.08 | 0.00033 | -0.00025 | 0 |
| 27' | Perpendicularity + dimensional tolerances | 0 | -2.80 | 0 | 0.01313 | 0 | 0.00445 |
| 29' | Flatness + dimensional tolerances | 1.14 | 0 | 0 | 0 | 0.00127 | 0.00132 |
| 30' | Perpendicularity + dimensional tolerances | 0 | -4.14 | 0 | 0.20414 | 0 | 0.00117 |
| 31' | Perpendicularity + dimensional tolerances | -0.30 | 0 | 0 | 0 | 0.00162 | 0.01105 |

**Table 7.** Nominal tolerance chain of the second KC.

| Chain | Description | matriks Roto-translation matrix | | | | | |
|---|---|---|---|---|---|---|---|
| | | Translation | | | Rotation | | |
| | | $d_x/\mu m$ | $d_y/\mu m$ | $d_z/\mu m$ | $d\theta_x/°$ | $d\theta_y/°$ | $d\theta_z/°$ |
| 1-2 | Nominal dimension + tolerance | 0 | 26499.5 | 0 | 0 | 0 | 0 |
| 2-3 | Nominal dimension + tolerance | 28249.3 | 0 | 0 | 0 | 0 | 0 |
| 3-4 | Nominal dimension + tolerance | 0 | 8499.9 | 0 | 0 | 0 | 0 |
| 4-5 | Nominal dimension + tolerance | 0 | 0 | 10000.3 | 0 | 0 | 0 |
| 5-6 | Nominal dimension + tolerance | 0 | 0 | 0 | 0 | 0 | 0 |
| 6-7 | Nominal dimension + tolerance | 19725.1 | 0 | 0 | 0 | 0 | 0 |
| 7-8 | Nominal dimension + tolerance | 0 | 0 | 77000.0 | 0 | 0 | 0 |
| 8-9 | Nominal dimension + tolerance | 0 | 0 | 0 | 0 | 0 | 0 |
| 9-10 | Nominal dimension + tolerance | 0 | 2999.8 | 0 | 0 | 0 | 0 |
| 10-11 | Nominal dimension + tolerance | 0 | 0 | 0 | 0 | 0 | 0 |
| 11-12 | Nominal dimension + tolerance | 0 | 0 | 38499.8 | 0 | 0 | 0 |
| 12-13 | Nominal dimension + tolerance | 6001.2 | 0 | 0 | 0 | 0 | 0 |
| 13-14 | Nominal dimension + tolerance | 0 | 0 | 0 | 0 | 0 | 0 |
| 14-15 | Nominal dimension + tolerance | 0 | 5999.7 | 0 | 0 | 0 | 0 |
| 15-16 | Nominal dimension + tolerance | 0 | 5999.5 | 0 | 0 | 0 | 0 |
| 16-17 | Nominal dimension + tolerance | 0 | 0 | 0 | 0 | 0 | 0 |
| 17-18 | Nominal dimension + tolerance | 0 | 0 | 55499.9 | 0 | 0 | 0 |
| 18-19 | Nominal dimension + tolerance | 0 | 24281.7 | 0 | 0 | 0 | 0 |
| 19-20 | Nominal dimension + tolerance | 34500.1 | 0 | 0 | 0 | 0 | 0 |

| 20-21 | Nominal dimension + tolerance | 0 | 29650.4 | 0 | 0 | 0 | 0 |
| 21-22 | Nominal dimension + tolerance | 40687.1 | 0 | 0 | 0 | 0 | 0 |
| 22-23 | Nominal dimension + tolerance | 0 | 0 | 0 | 0 | 0 | 0 |
| 23-24 | Nominal dimension + tolerance | 0 | 0 | 33000.0 | 0 | 0 | 0 |
| 24-25 | Nominal dimension + tolerance | 14811.7 | 0 | 0 | 0 | 0 | 0 |
| 25-26 | Nominal dimension + tolerance | 0 | 34717.9 | 0 | 0 | 0 | 0 |
| 26-27 | Nominal dimension + tolerance | 5023.7 | 0 | 0 | 0 | 0 | 0 |
| 27-28 | Nominal dimension + tolerance | 0 | 3650.8 | 0 | 0 | 0 | 0 |
| 28-29 | Nominal dimension + tolerance | 1075.0 | 0 | 0 | 0 | 0 | 0 |
| 29-30 | Nominal dimension + tolerance | 0 | 0 | 33000.0 | 0 | 0 | 0 |

**Table 8.** Variation tolerance chain of the second KC.

| Chain | Description | matriks Roto-translation matrix | | | | | |
| | | Translation | | | Rotation | | |
| | | $d_x$/μm | $d_y$/μm | $d_z$/μm | $d\theta_x$/° | $d\theta_y$/° | $d\theta_z$/° |
| 1' | Perpendicularity + dimensional tolerances | 0 | 0 | 4.91 | 0.00227 | 0.00108 | 0 |
| 2' | Perpendicularity + dimensional tolerances | 0 | -0.23 | 0 | -0.00640 | 0 | 0.00544 |
| 3' | Perpendicularity + dimensional tolerances | 3.33 | 0 | 0 | 0 | -0.00042 | 0.00692 |
| 5' | Flatness + dimensional tolerances | 0 | 0 | -2.04 | -0.00129 | 0.00007 | 0 |
| 6' | Perpendicularity + dimensional tolerances | 0 | 0 | -5.22 | -0.00006 | -0.00336 | 0 |
| 7' | Flatness + dimensional tolerances | 0 | -1.52 | 0 | -0.00280 | 0 | -0.00193 |
| 9' | Flatness + dimensional tolerances | 0 | 0 | -0.98 | 0.00736 | -0.00262 | 0 |
| 11' | Perpendicularity + dimensional tolerances | 0 | 0 | 0.02 | 0.01647 | 0.00473 | 0 |
| 12' | Perpendicularity + dimensional tolerances | 2.55 | 0 | 0 | 0 | 0.01108 | -0.00099 |
| 13' | Perpendicularity + dimensional tolerances | 0 | -1.82 | 0 | -0.01163 | 0 | 0.00068 |
| 15' | Perpendicularity + dimensional tolerances | 0 | 0.63 | 0 | -0.00500 | 0 | -0.00188 |
| 17' | Perpendicularity + dimensional tolerances | 0 | 0.25 | 0 | 0.00141 | 0 | -0.00016 |
| 18' | Parallelism + dimensional tolerances | 0.14 | 0 | 0 | 0 | 0.00077 | -0.00019 |
| 19' | Perpendicularity + dimensional tolerances | 0 | 0 | 0.30 | -0.00350 | -0.00033 | 0 |
| 20' | Flatness + dimensional tolerances | -1.63 | 0 | 0 | 0 | 0.00416 | 0.00156 |
| 23' | Perpendicularity + dimensional tolerances | 0 | 0 | 0.56 | 0.00410 | -0.00135 | 0 |
| 24' | Perpendicularity + dimensional tolerances | 0 | 4.92 | 0 | 0.01808 | 0 | -0.00903 |
| 26' | Flatness + dimensional tolerances | 0.70 | 0 | 0 | 0 | -0.00075 | -0.00017 |
| 27' | Perpendicularity + dimensional tolerances | 0 | 5.73 | 0 | 0.11331 | 0 | 0.00275 |
| 28' | Perpendicularity + dimensional tolerances | 4.62 | 0 | 0 | 0 | -0.00038 | -0.00488 |